Ultrasonic response of a brine-saturated reservoir rock during coupled stress and fluid perturbation during liquid-CO_2 injection

Chandra, Debanjan; Barnhoorn, Auke

DOI
10.1016/j.ijggc.2025.104498

Publication date
2025

Document Version
Final published version

Published in
International Journal of Greenhouse Gas Control

Citation (APA)
Chandra, D., & Barnhoorn, A. (2025). Ultrasonic response of a brine-saturated reservoir rock during coupled stress and fluid perturbation during liquid-CO_2 injection. *International Journal of Greenhouse Gas Control*, *147*, Article 104498. https://doi.org/10.1016/j.ijggc.2025.104498

International Journal of Greenhouse Gas Control 147 (2025) 104498

Contents lists available at ScienceDirect

International Journal of Greenhouse Gas Control

journal homepage: www.elsevier.com/locate/ijggc

Ultrasonic response of a brine-saturated reservoir rock during coupled stress and fluid perturbation during liquid-CO_2 injection

Debanjan Chandra [a,b,*], Auke Barnhoorn [a]

[a] Department of Geoscience and Engineering, Delft University of Technology, Stevinweg 1, 2628 CN Delft, the Netherlands
[b] Department of Geosciences (IGV), Norwegian University of Science and Technology (NTNU), S. P. Andersens veg 15a, 7031 Trondheim, Norway

ARTICLE INFO

Keywords:
Near-well monitoring
CO_2 storage
Ultrasonic velocity
Stress forecasting
Plume migration
Triaxial failure

ABSTRACT

CO_2 injection into porous sandstone reservoirs offers a promising pathway to curb anthropogenic carbon emissions, but poses risks of leakage and induced seismicity from stress perturbations and fault reactivation without meticulous monitoring. Here, we present a time-lapse monitoring approach based on laboratory measurements of ultrasonic Vp, Vs and corresponding peak amplitudes in critically stressed, partially saturated North Sea sandstones (porosity 9–23%). Our experiments show that Vp and Vs exhibit higher sensitivity (4–15%) to stress changes compared to fluid saturation changes (0.8–1%), whereas amplitudes are more responsive (30–500%) to saturation, showing staggered change when brine is displaced by CO_2. Under pure stress perturbation, amplitude variations are smaller (10–50%). During elastic deformation, the Vp/Vs ratio decreases while the ratio of their corresponding amplitudes increases, underscoring the need for both P- and S-wave measurements. Velocity and amplitude changes are more pronounced in high-porosity rocks. In a critically stressed state (beyond yield/before failure), the rise in pore fluid density from CO_2 injection boosts shear wave amplitudes, offsetting attenuation from inelastic deformation. Knowing the pre-injection stress state enables these velocity and amplitude trends to serve as robust indicators of reservoir conditions during and after CO_2 injection. This cost-effective approach can be adapted to reservoir-scale monitoring and extends beyond CCS, supporting enhanced detection of stress and fluid-induced changes in subsurface formations.

1. Introduction

Subsurface CO_2 storage (CCS) is gaining accelerated growth worldwide as governments and industry solidify their commitment to atmospheric CO_2 abatement (Bui et al., 2018; Y. Zhang et al., 2022). Depleted oil and gas reservoirs are relatively well studied due to their history of hydrocarbon production and are therefore identified as primary targets for storing CO_2. However, CO_2 injection operation is complicated and comes with its own risks including possibility of leakage, wayward plume movement, risk of fault reactivation etc. to name a few. Therefore, extensive studies are performed both in laboratory and reservoir scale prior to injection to ensure safe containment of CO_2 for a considerably long period. The short term and long-term effects of CO2 on mechanical properties of sandstones along with its velocity signature have been explored in recent years (Cerasi et al., 2018; Hangx et al., 2013; Hu et al., 2017; Kim and Makhnenko, 2022; Ranjith and Perera, 2011; Tarokh et al., 2020; Van Stappen et al., 2018; Xing et al., 2019; Zhang et al., 2021; Zheng et al., 2015), which report permanent alteration in mineralogy, porosity, permeability and fracture aperture (for fractured rocks) depending on the experimental timescale, pressure, temperature and phase of CO_2 (gas, liquid or supercritical). Monitoring tools used during and post injection also ensure if the CO_2 plume and reservoir both are behaving in an expected manner (Feng, 2017; Furre et al., 2017; Will et al., 2014).

Evolution of stress-state is a key parameter to monitor during a CO_2 injection operation, which is directly affected by continuous build-up of CO_2 pressure in the reservoir. In the subsurface direct measurement of stress is tricky and often other proxies are used to infer stress state in the reservoir such as InSAR data, strainmeter, tiltmeter etc., which provide regional or local reservoir or ground deformation (Furst et al., 2020; Murdoch et al., 2020; T. Zhang et al., 2022). Geophysical monitoring using seismic interferometry and 3D seismic imaging, using conventional tools and optic fibers are periodically performed to track CO_2 plume movement in the subsurface (Bachrach et al., 2023; Feng, 2017;

* Corresponding author at: Department of Geosciences, Norwegian University of Science and Technology (NTNU), S. P. Andersens veg 15a, 7031 Trondheim, Norway.
E-mail address: debanjan.chandra@ntnu.no (D. Chandra).

https://doi.org/10.1016/j.ijggc.2025.104498
Received 18 February 2025; Received in revised form 11 July 2025; Accepted 8 October 2025
Available online 15 October 2025

Furre et al., 2017; Gasperikova et al., 2022), while microseismicity monitoring is performed to track any indications of induced seismic activity (Will et al., 2014). However, these monitoring techniques are expensive, which leads to an increased project expense. Compressional and shear wave velocity measurement have proven to be sensitive to both stress change (Barnhoorn et al., 2018; Chandra et al., 2024; Dutta et al., 2020; Sang et al., 2020; Sayers and Kachanov, 1995; Veltmeijer et al., 2024; Zotz-Wilson et al., 2019) and CO_2 plume movement in the subsurface (Agofack et al., 2018; Falcon-Suarez et al., 2020; Fortin et al., 2005; Guéguen and Schubnel, 2003; Hamada and Joseph, 2020), which can be leveraged to effectively monitor safe disposal of CO_2 into the subsurface. Lab scale experiments on the effect of fluid saturation and stress change on ultrasonic and seismic velocity have been explored before, which mostly govern the relationship between degree of saturation and velocity, but limited studies have been conducted to explore the coupled impact of stress and saturation change in porous reservoirs (Hughes and Kelly, 1952; Janssen et al., 2021; King and Marsden, 2012; Li et al., 2022; Meglis et al., 2005; Scott et al., 1993; Stanchits et al., 2003; Yamabe et al., 2016; Zhu et al., 2022; Zhubayev et al., 2016).

Irreversible deformation of reservoir rocks, which is detrimental for safe operation, cause reduction of Vp and Vs. However, such velocity reduction can also be caused by displacement of reservoir brine by CO_2 due to the difference in density of both fluids (Gassman, 1951; Nur and Simmons, 1969), which is an integral part of CO_2 injection. Therefore, without proper benchmarking, change in wave attributes can raise false alarm during CO_2 injection. Previous studies so far have illustrated the effect of CO_2 saturation and plume movement on wave propagation both from field scale and laboratory observations. Alemu et al., (2013) found that at low CO_2 saturation, P wave amplitude is more sensitive and as saturation increases, the change in wave amplitude is minimal due to energy loss between interfaces of brine and CO_2 saturated pores. Although the Gassman equation and its derivatives can predict the change in velocity and elastic modulus as a function of fluid saturation (Berryman, 2012; Diallo et al., 2003; Mavko and Nolen-Hoeksema, 2012a; Sevostianov, 2020), this doesn't account for the associated stress change in the reservoir.

In this study we simulate a CO_2 injection operation in a critically stressed (i.e beyond yield stress and before failure) brine-saturated sandstone coreplug to study how the ultrasonic wave attributes respond to stress change, fluid displacement and a coupling of both these factors. The experimental protocol adopted for this study emulates a situation where CO_2 is injected in a saturated and critically stressed saline aquifer. Since the principles discussed in this study will be somewhat similar for depleted oil and gas reservoirs as well, we will use the term 'reservoirs' going further to represent a broader array of potential CO_2 reservoirs. Understanding the change in elastic wave properties during the lifecycle of CO_2 injection is the primary objective of this study, where both fluid displacement and stress perturbation influences the ultrasonic wave attributes. Our aim is to find out how the contribution of stress and fluid invasion can be isolated by looking at wave attributes in a simplistic CO_2 injection case in order to establish elastic wave properties as an effective monitoring tool in a field scale scenario.

2. Methodology

2.1. Sample preparation

The core samples used in this work (Table 1) are sourced from different depths of the Aramis CO_2 storage license area in the North Sea (https://www.aramis-ccs.com). This is a depleted gas field where the reservoir rocks are primarily sandstone. The sandstone coreplugs were provided by Shell through TNO (Nederlandse Organisatie voor Toegepast Natuurwetenschappelijk Onderzoek). The geology of the area is well studied (De Jager and Geluk, 2007; Geluk and Röhling, 1997) and the geological maps as well as well logs are openly available through NLOG (https://www.nlog.nl/). Air permeability of studied depth intervals (or close) measured at 400 bars are reported from NLOG data repository. The collected samples belong largely to Upper and Lower Slochteren and middle Solling formation from offshore Netherlands. The middle Solling Formation consists of fine to medium well sorted sand grains formed by Eolean dune deposit. It has a high porosity, permeability and low heterogeneity (Filomena et al., 2012). The upper Slochteren with dominant sabkha facies on the other hand has impaired areas due to low permeability and a high heterogeneity (Van Hulten, 2006). The Lower Slochteren Formation has high degree of burial diagenesis and salt deposition in some depth intervals, causing heterogeneity in porosity and permeability (Van Hulten, 2006). The collected samples were first trimmed and polished to maintain parallel end faces with a final diameter of 1 ± 0.1 inch and length of 2 ± 0.1 inches. The finished samples were further dried at 60°C in an oven for 24 hrs and then their porosity and grain density were measured with a helium pycnometer. The samples were then vacuum saturated in a low salinity brine solution (80 g/L NaCl) for 24 hrs to allow maximum brine saturation before the experiments.

2.2. Experimental protocol

The experiment was planned in a way to closely represent the stress change in a critically stressed depleted saline aquifer during CO_2 injection. In the case of a saline aquifer, when CO_2 is injected into the reservoir, it displaces the brine from the pore spaces and increases the pore pressure simultaneously. When the reservoir is critically stressed, too much pore pressure buildup can initiate plastic deformation in the reservoir rock, which is often identified by a deviation from linearity in the stress-strain profile, resulting in irreversible deformation within the reservoir preceding failure. In this stage, microcracks start appearing, weakening or damaging the reservoir.. The sandstone coreplugs saturated in brine (section 1.1) were loaded into a custom-made Hoek cell which is able to apply confining pressure onto the coreplug. The Hoek cell was then connected to a 500 kN uniaxial loading frame, which can apply axial load (Fig. 1). For these experiments, load was applied by constant upward movement of the bottom platen of the load frame with a slow rate of 0.2 μm/s. The rate of movement was controlled by two Linear Variable Differential Transformers (LVDTs) with a maximum displacement of 2 mm connected to both ends of the bottom platen (Fig. 1a). The stainless-steel pistons connected to the top and bottom of

Table 1
Samples used for this study along with their origin, connected porosity and grain density. The permeability values are extracted from NLOG.

Well ID	Formation	Sample name	Depth (m)	Porosity	Permeability* (mD)	Grain density (g/cc)
K15-12	Upper Slochteren	K15–12-5V	3930.05	0.11	0.32	2.71
K15-FG-102	Upper Slochteren	K15-FG–102-3V	4176.8	0.17	3.2	2.69
L09-10	Solling	L09–10-7V	3172.2	0.23	933	2.55
L09-10	Solling	L09–10-16V	3212.2	0.13	69	2.62
K15-15A	Lower Slochteren	K15-15A-7V	4236.18	0.11	72.9	2.75
K15-15A	Lower Slochteren	K15-15A-8V	4236.81	0.09	66.1	2.73
K15-15A	Lower Slochteren	K15-15A-12V	4249.3	0.14	0.18	2.73

* Permeability for exact same depth intervals were not present in most cases, therefore corresponding permeability of closest possible depth having similar porosity was reported.

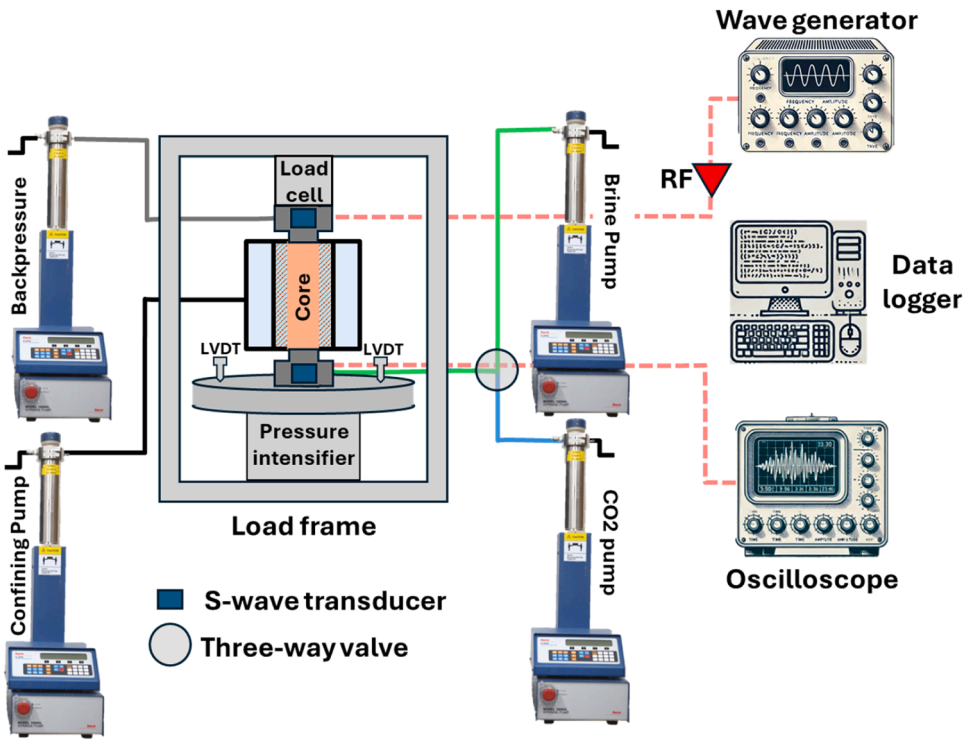

Fig. 1. Experimental setup used for this study containing the loading, flow and sonic measurement system.

the sample was also custom-made and each of them houses a 1 MHz S wave transducers of 5 mm diameter. The pistons also allow fluid flow through them without affecting wave propagation. Porous meshes were used between the sample and piston in both ends to ensure even distribution of fluid on each end of the coreplug. One of the S wave transducers was connected to the wave generator through an amplifier, which acted as the source and the transducer on the other end of the coreplug acted as a receiver which was connected to an oscilloscope and datalogger to automate saving of waveforms. A small component of the shear wave energy converts to compressional wave at the contact between anisotropic media (in this case between transducer-piston-specimen), resulting in small vertical displacement. This converted mode is recorded at the receiver and attributed as the P wave arrival time for the experiments. Technical specifications of the acoustic setup can be found in (Veltmeijer et al., 2024). It is worthwhile to mention that the ultrasonic waveforms were recorded every 10 s for 500 μs and averaged over 128 stacks for an enhanced signal-to-noise ratio. A sampling frequency of 2 MHz was used for recording the waveforms, which resulted in a 0.5 μs picking error in P and S wave arrival times for each experiments. Waveforms collected during the experiments were processed with Radex Pro software to pick Vp, Vs, P wave amplitude (Pamp) and S wave amplitude (Samp). Pamp and Samp represent the highest amplitude of a 10 μs symmetric window around the P and S wave arrival time. The Vp and Vs were calculated after deducting the travel time of the pistons. A total of four ISCO 100DM syringe pumps were used to apply fluid pressure in the system. One of the pumps was used for building confining pressure. The outlets of two pumps (one for 80 g/L NaCl brine and another for pure liquid CO_2) were connected with a three way valve, which was further connected to the bottom piston for pore fluid injection so that only one fluid can be injected at once. One pump was connected to the top piston for applying backpressure and also to monitor pore fluid pressure buildup in the sample.

All pore fluid lines were made from ¼ inch stainless steel tubes with a cumulative dead volume of 7 ml. To represent the stress condition of an intermediate-depth CO_2 storage reservoir (1–2 km deep), a hydrostatic stress of 40 MPa is selected as the starting point of the experiment. The experiments were conducted in the following steps (as indicated in Fig. 2a, b):

a. We built a 40 MPa hydrostatic load at 10 MPa/min rate. 20 pore volume (PV) of brine was injected into the sample at 5 ml/min and was allowed to bleed from the downstream line. This step ensured maximum escape of air (if any) from the flow lines or sample. The top piston was connected to the backpressure pump to build a constant nominal pore pressure of 0.1 MPa. A thin layer of viscous ultrasound gel was applied between the piston-sensor and piston-sample contact (in both pistons) for uniform transmission of waves. The parallel end faces of the coreplugs ensured even load distribution and optimum contact between sample and pistons.
b. Timelapse ultrasonic velocity measurement was started along with axial stress buildup by constant upward movement of the bottom platen at 0.2 μm/s. The stress-strain profile was closely monitored till the stress profile started changing its slope (start of plastic deformation). At this point, the loading mechanism was changed from deformation controlled to load controlled. This allowed the machine to maintain a constant axial stress and adjust piston movement accordingly.
c. The brine injection pressure was raised up to 6 MPa at 1 MPa/min rate. The pressure was selected to represent a depleted aquifer and also since liquid CO_2 (which is the displacing fluid) is unstable below 6 MPa at laboratory temperature. The laboratory was centrally heated to maintain a constant temperature of 19°C, which is below the boiling point of pure CO_2 (21.6°C) at 6 MPa. The experimental setup was covered with a thick insulating cover to minimize influence of sudden temperature changes. A room thermometer was placed close to the sample enclosure to monitor any changes. While CO_2 stays in supercritical phase within the reservoir, due to lack of heating module in our experimental setup and to avoid the freezing effect due to the liquid-supercritical transition of CO_2, we selected liquid CO_2 as our pore fluid. We discuss later, how the observations might vary when supercritical CO_2 is used as pore fluid instead of liquid CO_2. It is worthwhile to mention that the samples tested are

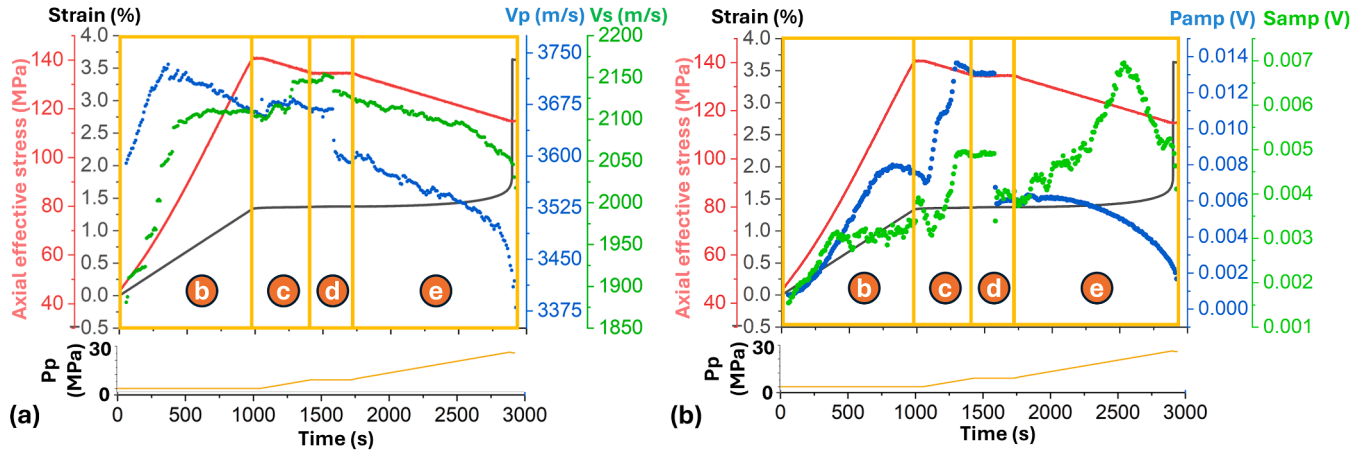

Fig. 2. An experiment with different stages indicated in circles (description in text) along with (a) Vp and Vs measurement and (b) Pamp and Samp measurement. The mini plots below each figure indicates pore pressure development over time. Pp indicates pore pressure.

highly porous and permeable which ensured that the pressure difference between upstream and downstream pump never exceed 0.5 MPa. Once desired pressure is achieved, wait for pressure to equilibrate.

d. A liquid CO_2 pressure of 6 MPa was built up to the three-way valve, and further allowed to flow into the plug by turning the valve. A drawdown rate of 5 ml/min was applied in the backpressure pump causing a slow drop in line pressure and allowing CO_2 to flow into the sample. After drawdown of 30 PV, we assumed that the coreplug is mostly saturated with CO_2 and some brine (similar to reservoir scenario).

e. The drawdown was stopped from backpressure pump and CO_2 inlet pressure started increasing at 1 MPa/min and continued until the sample fails.

3. Results

In stage B (for nomenclature of the stages refer Fig. 2) as the axial stress is increased, both Vp and Vs increase uniformly during elastic deformation stage, followed by a nearly identical rate of decrease since the onset of plastic deformation (Fig. 3).

Interestingly, Vp of the sandstones from L09 well doesn't show

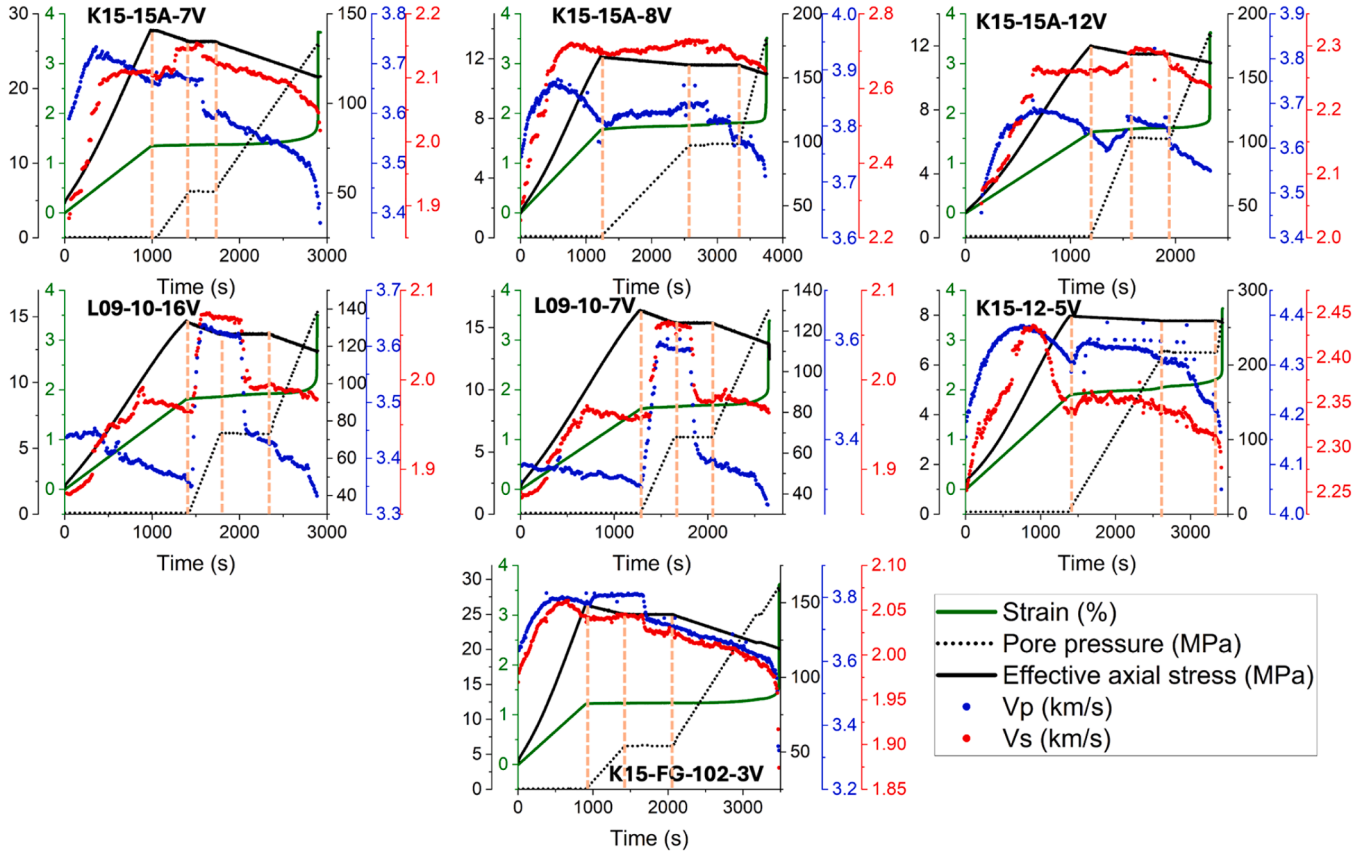

Fig. 3. Change in Vp and Vs as a function of stress change and fluid displacement until the point of failure during the triaxial tests. The dotted orange vertical lines indicate transition stages 'b' through 'e' of each experiment.

significant increase during the loading stage, which follows the Mori-Tanaka relationship and experimental study by David and Zimmerman, (2012) and is commonly observed in saturated high-porosity rocks. Since the start of brine injection in stage c, both Vp and Vs show minimal change in the beginning and only after the fluid pressure reaches 1–2 MPa, there is a sudden and significant increase in the velocities. It is to be noted that for low porosity samples (e.g K15-12-5 V and K15-15A-8 V), despite maintaining a constant rate of pressure increase, a longer time was allowed for the differential pressure across the coreplug to reach close to 0.1 MPa to ensure pressure equilibrium in the whole specimen. After the pore pressure reaching 6 MPa, liquid CO_2 is flushed through the sample (stage d) which at first causes minor drop in velocity when the coreplug is partially saturated with CO_2, followed by a rapid drop in velocities due to lower density of liquid CO_2 compared to brine (Fig. 3). In the last stage of the experiment (stage e), liquid CO_2 pressure is increased at a uniform rate, which causes a decrease in velocities as the pore pressure starts opening microcracks and induces new crack formation in the critically stressed coreplugs. Continuing pore pressure increase increases the rate of axial deformation and in moments preceding failure, the axial strain exponentially increases. Vp and Vs concurrently decreases rapidly when the axial strain increases fast, signifying axial failure of the specimen. In general, change in Vp is more pronounced with pore pressure increase compared to change in Vs. For K15-12-5 V, the failure occurred after minimal CO_2 pressure increase and therefore the number of datapoints for that experiment are fairly less than the other samples.

Similar trend can be seen for Pamp and Samp in different stages of the experiments. Both of them show high sensitivity with pore pressure increase and CO_2-brine displacement compared to stress change (Fig. 4). Interestingly in stage e, the amplitudes behavior differently from the velocities. The amplitudes, especially Samp increase as the CO_2 pressure increases with only exception being in low-porosity samples (K15-15A-8 V and K5-12-5 V).

The increasing trend for Samp and in some cases Pamp in stage e continues as long as there is minimal change in axial strain. As soon as the coreplug approaches failure and axial strain increases exponentially, both Pamp and Samp drops.

4. Discussion

For ease of understanding we subdivide the experiments in four stages (b-e) to discuss the key finding in each stage as follows. We skip discussing stage A, where only hydrostatic loading is performed to bring the axial and confining stress to 40 MPa.

4.1. Stage B–approaching critical stress conditions

Starting from hydrostatic stress condition, axial stress increment also causes increase in Vp, Vs and their corresponding amplitudes (Fig. 3, 4), barring samples belonging to L09 well, where there is negligible increase in Vs and especially Vp. The rate of increase in Vp and Vs is also strongly dependent on porosity as validated by Chandra et al., (2025). Interestingly, the change in Vp and Vs or their amplitude does not happen at the same rate even within the same coreplug. Up to 100 MPa, all of the coreplugs go through elastic deformation and in that period Samp/Pamp drops sharply (Fig. 5a) (except K15-12-5 V). A linear rescaling method was adopted to normalize the Samp/Pamp and Vp/Vs values. For example, minimum Samp/Pamp value for each experiment is considered as 0, whereas the maximum value is considered to be 1. This method preserves the relative spacing of the values and makes comparing parameters across different samples easier. Similar normalizing scheme is used in all following instances.

During this phase the Vp/Vs ratio also drops (Fig. 5b) which indicates relatively faster increase in Pamp compared to Samp but slower

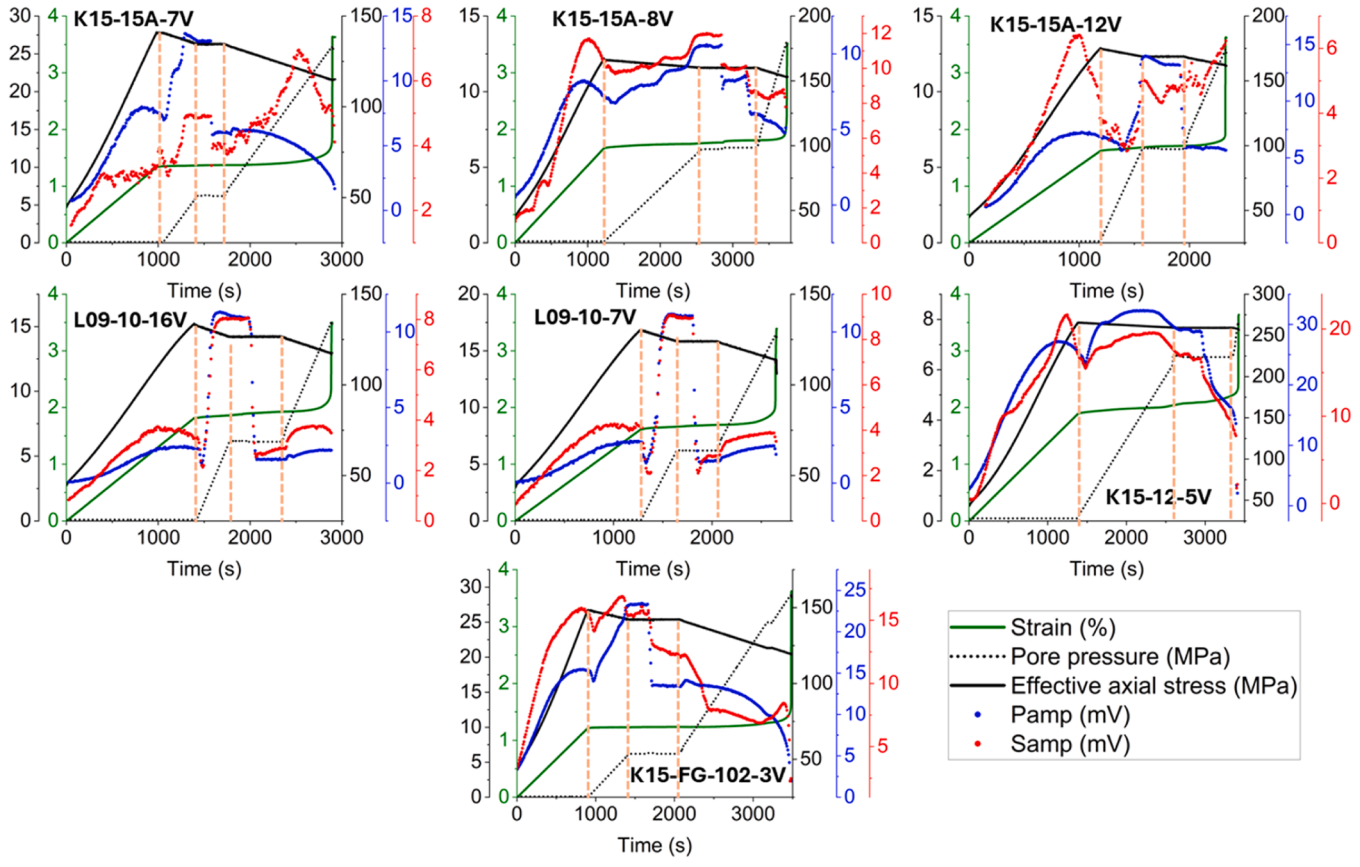

Fig. 4. Change in Pamp and Samp as a function of stress change and fluid displacement until the point of failure during the triaxial tests.

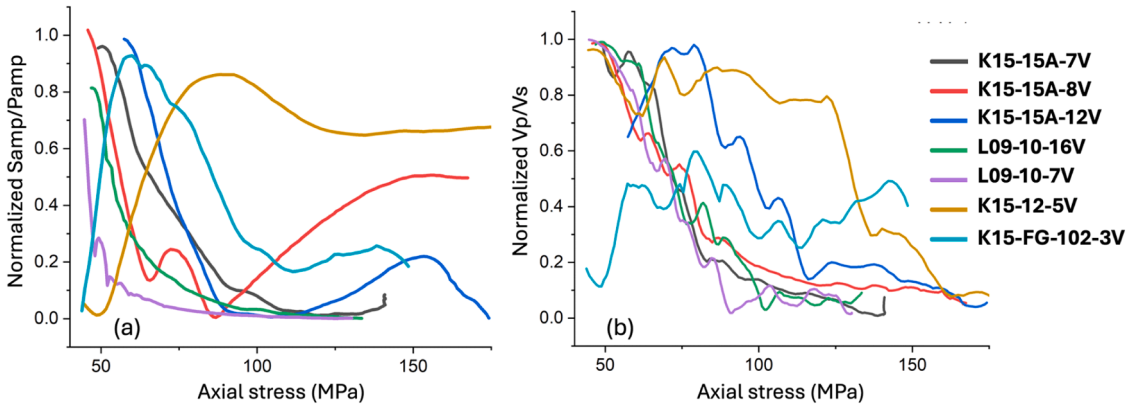

Fig. 5. (a) Normalized Samp and Pamp ratio and (b) Normalized ratio of Vp and Vs as a function of axial stress during the axial loading phase of the experiment.

increase in Vp compared to Vs. While transitioning into plastic deformation, there is a subtle trend reversal in Samp/Pamp, where increase in Samp happens faster than Pamp (Fig. 5a). However, there is no such trend reversal in the Vp/Vs ratio. Transitioning into plastic deformation, Vp/Vs maintains the decreasing trend, however the rate of decrease is slowed down significantly.

4.2. Stage C-approaching depleted reservoir condition

In this stage we start increasing the pore pressure in the coreplug

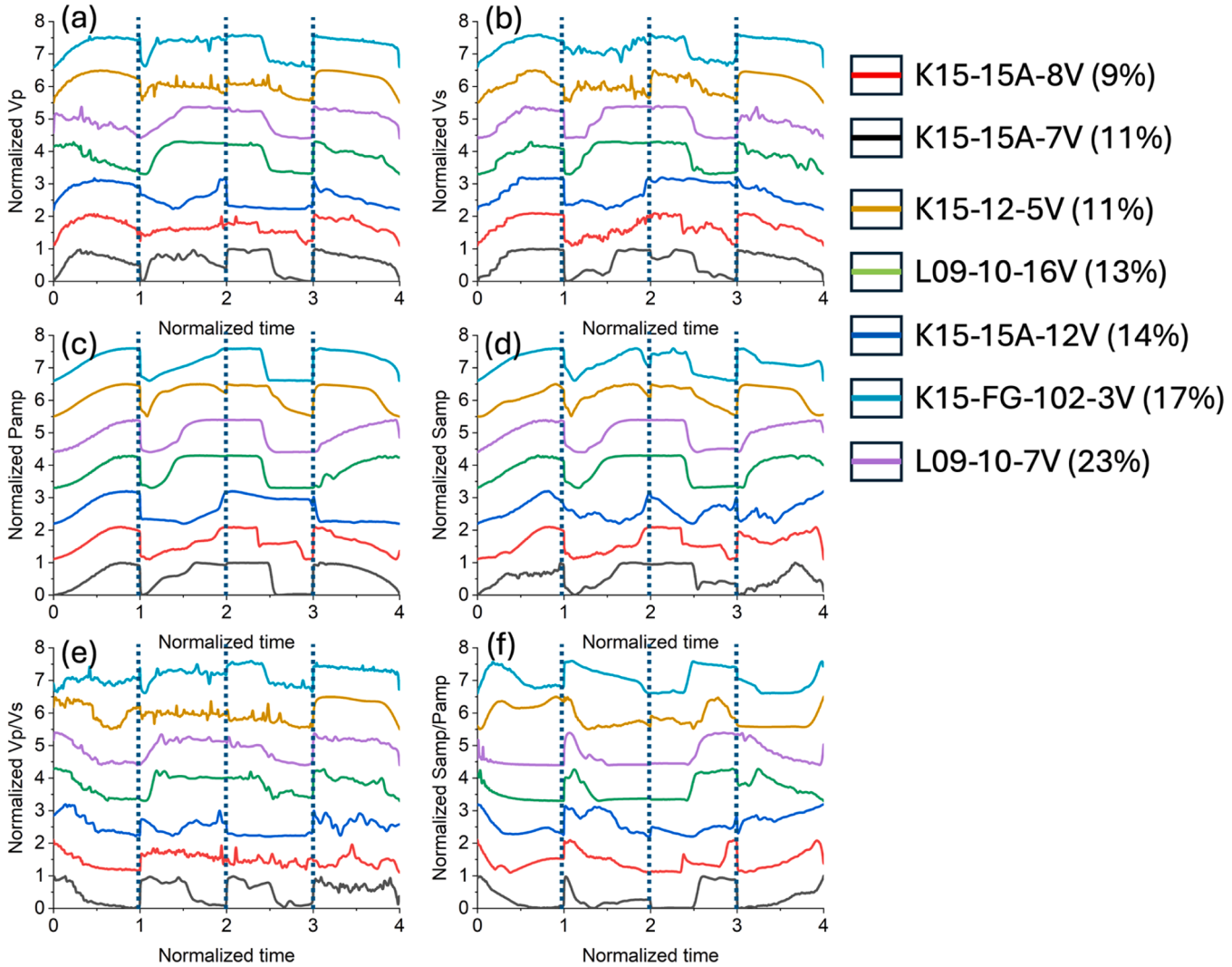

Fig. 6. Change in different ultrasonic attributes throughout the experiments (a) Vp, (b) Vs, (c) Pamp, (d) Samp, (e) Vp/Vs, (f) Samp/Pamp. Each experiment is divided into 4 parts following the protocol mentioned in Fig. 2. Values of sonic attributes and time are normalized within each part of the experiment for better comparison across all samples.

with NaCl solution while the axial and radial stresses are kept constant. The samples are allowed to deform freely as long given the constant stress. In theory, increase of the pore pressure within the elastic limit of the coreplug will lead to an increase in Vp and Vs due to increasing density of pore fluid contained within the pores. A higher pore pressure will also allow filling of more pore spaces, which might have remained unsaturated during the vacuum saturation stage. Interestingly, despite a constant increase in pore pressure, the change in velocity in this stage is abrupt. Up to almost 3 MPa pore pressure, the velocity increase is slow, and suddenly halfway through, there is a sudden increase in Vp, Vs and their corresponding amplitudes (Fig. 6). This abrupt change in velocities is validated by earlier studies on anisotropic geological samples with complex pore structure (Berryman, 2004; Knight et al., 2012; Lebedev et al., 2009; Zhang et al., 2017) described as patchy saturation model which doesn't quite follow the Gassman-Wood or Gassman-Hill trends. This phenomenon occurs due to differential saturation of the porous rock when fluid pressure starts to increase at the upstream, depending on the permeability, the downstream end is still at a lower pressure and therefore not completely saturated. Due to dispersion of waves at the interface of partially and fully saturated part of the coreplug, the velocities and amplitudes show minimal change in the beginning. When the fluid pressure increases from one end, the fluid front progresses further, saturating more pores, which results in an increase in velocity and amplitudes. Depending on the complexities of flow paths, the increase in velocity and amplitude is stepped or gradual. Since the measurements are conducted with high frequency waves, the delayed velocity response can also be explained by capillary pressure equilibrium theory (Dasgupta et al., 2024; Qi et al., 2014b; Sen and Dvorkin, 2013), which follows similar principle as squirt flow (Gurevich et al., 2010; Ógúnsàmi et al., 2025; Sun, 2021; Sun et al., 2020). The capillary pressure-based model assumes a heterogeneous media, which is composed of multiple patches with different porosity, permeability and capillary threshold in each patch. In each patch, capillary forces resist rapid fluid movement, which delays the equilibrium. Until then, the velocity and amplitude responses remain in transitional state and do not reflect the new fluid configuration. Both capillary pressure-based model and squirt flow justify the hysteresis in the velocity-saturation trends, causing decoupling between stress state and immediate acoustic response, which is evident in stage B and C for all experiments (Fig. 6). However, in order to quantitatively discern the effect of capillary pressure-based model, degree of heterogeneity needs to be measured across the coreplug at a resolution smaller than the characteristic wavelength (smaller than $\sim$ 3.3 mm for these set of samples), and such microstructural analysis is beyond the current scope of study. It is worthwhile to mention that there is a small drop in the velocity and more observable drop in amplitude when the brine injection starts (Fig. 4, 5). Given that the pressure front moves faster than the fluid front in complex porous materials (Brantut and Aben, 2021; Chapman et al., 2021), and considering that the rock is already in plastic deformation zone, even slight increase in pore pressure induces more microcracks in the coreplug, which further attenuates compressional and shear waves through the media. The minimal change in Vp/Vs ratio during this stage indicates that the wave velocities increase by the same proportion. However, the Samp/Pamp ratio decreases steadily during the pore pressure buildup. There is also considerable research performed on the evolution of velocities as a function of injection rate (Lopes et al., 2014; Lopes and Lebedev, 2012; Qi et al., 2014a), however in our present study, we set control on the rate of fluid pressure while the injection rate was allowed to change freely.

4.3. Stage **D**-effect of fluid displacement on wave propagation

In this stage of the experiment, we start pushing liquid CO_2 (lCO_2) through the coreplug at a constant upstream pressure and by applying 5 ml/min drawdown rate with the backpressure pump. As expected, due to the lower density of liquid CO_2 than brine, the velocity and amplitudes decrease during the fluid displacement phase. In a reservoir scale CO_2 injection operation, we expect this situation in the beginning, where CO_2 injection only displaces the brine partially out of the pores (depends on the wettability of the pores) with minimal influence on pressure. Similar to stage C, in this case also, the velocity and amplitude response is a bit delayed (Fig. 6). Generally, in CCS projects, depending on the gradient between injection pressure and initial pore pressure, CO_2 injected in liquid state gets converted to supercritical state. However, to achieve experimental simplicity, we chose the pressure conditions in such a way to avoid phase change or freezing effect involved with liquid to supercritical transition of CO_2, and also at the experimental timescale, the reactivity of CO_2 with brine or host rock is assumed to be minimal. Since the pressure is kept constant during the fluid displacement, we assume no further deformation in the coreplug takes place. The late and sudden drop in velocity and amplitude can be attributed to the patchy saturation model discussed in the previous subsection. Other attributes like Vp/Vs and Samp/Pamp show opposite trend of the previous stage, i.e the Vp/Vs ratio drops and Samp/Pamp ratio increases synchronously to the change in velocities.

4.4. Stage E-pore pressure increase leading to failure

In this final stage, we increase the pore pressure keeping the axial and radial stresses constant and this is where the deformation and velocity has a complex relationship. On one hand increase in liquid CO_2 pressure increases the density of pore fluid, resulting in faster wave propagation (Janssen et al., 2023), whereas the increasing plastic deformation in the coreplug due to increasing pore pressure attenuates wave propagation. Risk of failure due to pore pressure injection is well documented in previous studies using experimental and numerical approach (Damani et al., 2018; Frempong et al., 2007; Komijani et al., 2019; Mayr et al., 2011; Rafieepour et al., 2021). In these experiments the start of pore pressure increase immediately leads to a decrease in Vp and Vs, signifying that inelastic deformation plays a major role in governing the velocity change during pore fluid injection. Similar velocity change due to inelastic deformation was also observed in Stage B, however, the deformation was caused only due to axial loading. Upon comparing the change in velocities due to inelastic deformation in both Stage B and E, we found generally higher magnitude of change in Stage E compared to Stage B (Fig. 7a, b), which is intuitive, since more inelastic deformation close to failure occurs in the last stage. However, this also means that presence of liquid CO_2 in the pore spaces doesn't slow down the rate of decrease in velocities. Magnitude of change in Vs for K15-12-5 V was higher in Stage B already, due to more inelastic deformation incurred (as discussed in section 3), hence we did not consider those datapoints for linear regression fit. Interestingly, with increasing porosity, the magnitude of velocity drop also increases for both Vp and Vs. Conversely, Pamp and Samp shows a reverse trend, where higher porosity reduces the magnitude of change in amplitudes (Fig. 7c, d). We can get a clue for such behavior also from Fig. 4, which indicates that if inelastic deformation attenuates wave amplitudes, the increasing pressure and density of pore fluid tries to increase the amplitudes. Finally, close to failure, the amplitudes decrease rapidly as it cannot keep up with the exponentially increasing crack volume (indicated by the axial strains in Fig. 4). Coming now to Fig. 7c, higher porosity indicates higher volume of liquid CO_2 in the pore space, which contributes to a subtler change in Pamp. On the contrary, in low porosity samples, where waves travel mostly through the matrix, increasing volume of cracks considerably bring down the amplitudes, and the pore fluid density has minimal role to play.

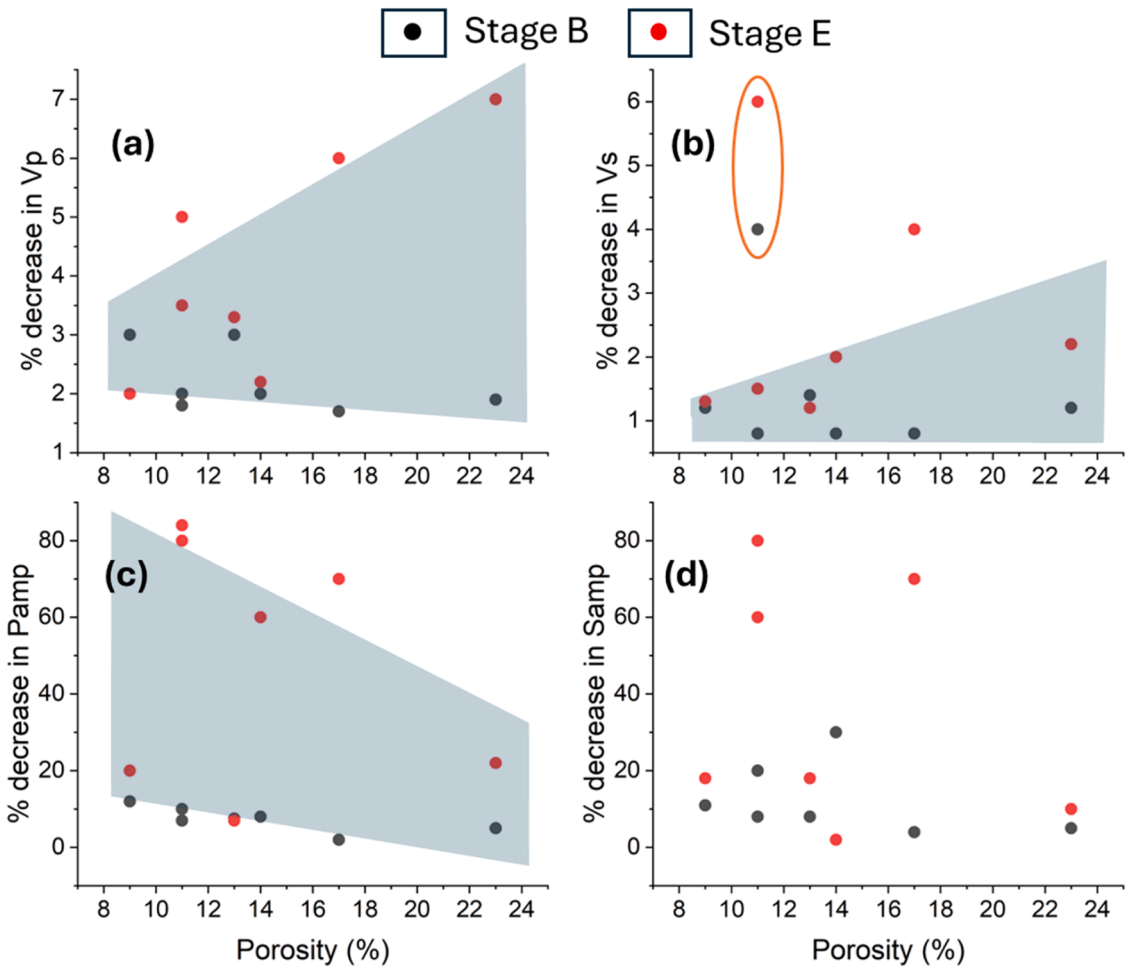

Fig. 7. Comparison of the percentage decrease in sonic attributes (a) Vp, (b) Vs, (c) Pamp and (d) Samp in Stage B and Stage E of the experiments. The circled dataset in (b) belongs to K15-12-5 V. The color-filled region represents the area between the linear regression fits of Stage B and E datasets. Due to lack of strong linear fit, there is no such region marked in (d).

4.5. Applicability for reservoir monitoring at seismic frequency

Different forms of seismic monitoring are widely used for monitoring plume migration in CO_2 storage complexes. Leveraging the difference in acoustic impedance of reservoir brine and injected CO_2, migration of CO_2 in the subsurface can be traced. Although combining other forms of monitoring (e.g resistivity, electomagnetic) provides better resolution (Fawad and Mondol, 2021), but might drive up the monitoring significantly (Mathieson et al., 2011). In a unique field-scale controlled CO_2 leakage experiment (Michael et al., 2020) found that the change in CO_2 plume is clearly detectable in downhole seismic measurements. Vertical seismic profiling (VSP) along with surface seismic measurement is currently used extensively for monitoring plume migration near injection well. Effectiveness of surface seismic to monitor CO_2 plume migration was demonstrated by Arts et al., (2004) in Sleipner. Timelapse VSP was also used in the Frio Pilot well to monitor CO_2 plume near injection well (Daley et al., 2007, 2008a), whereas a more cost effective permanent and semi-permanent deployment was setup in Penn-West and Otway Project respectively (Chalaturnyk et al., 2006; Daley et al., 2008b; Lawton et al., 2006), which additionally also provides opportunity for microseismic monitoring. 2D and 3D VSP monitoring is also successfully implemented in Weyburn, Decatur, and SACROC project (White et al., 2021). Techniques like crosswell seismic monitoring is deployed to get around the lack of resolution in traditional VSP monitoring. Permanent or semi-permanent continuous crosswell monitoring has also been used successfully in Cranfield, Aquistore, Frio Pilot and Nagaoka Pilot, which could monitor changes in CO_2 plume at a high spatial and temporal resolution based on velocity change in the subsurface. Using a combined reservoir simulation, rock physics and synthetic seismic workflow, Eid et al. (2015) was able to robustly detect CO_2 plume growth and overall migration, especially when there are structural baffles creating accumulations. However, their approach had considerable uncertainty while inverting for exact saturation due to the uncertainty in extent of heterogeneity. Many other studies (L. Hu et al., 2017; Huang et al., 2018; Ivandic et al., 2018; Kolkman-Quinn et al., 2023; Picotti et al., 2012; Wang et al., 2020; Zhu et al., 2019) have expressed similar uncertainty while inverting for exact CO_2 saturation using different approaches including timelapse 3D seismic, borehole seismic, and synthetic seismic simulation using direct arrivals, AVO (amplitude versus offset) or coda waves. The degree of uncertainty rises when the reservoir is highly heterogeneous and depends on sensor coverage, their proximity to plume and repeatability of the active seismic sources.

Although several instances of plume migration monitoring are well documented with long-term field scale application, there is no evidence of direct stress monitoring using calibrated velocity data. Prasad et al. (2021) highlighted that with information of crack density, soft grain contact and experimental data on stress-velocity relationship, pressure change within the reservoir can be quantified. Chandra et al. (2025) already demonstrated quantification of crack density from ultrasonic P and S waves in laboratory scale. Several experimental studies exist that attempts to bridge the gap between ultrasonic and seismic scale stress

and saturation-dependent velocity changes.

For saturated porous sedimentary rocks, previous studies have pointed out considerable acoustic dispersion when comparing ultrasonic and seismic frequency measurements (Chapman et al., 2019, 2016; Nur and Simmons, 1969; Pimienta et al., 2015). It is postulated that in a global scale, flow dispersion in saturated media arises due to the forced motion of the fluid caused by induced waves. This flow dispersion is usually caused by low-frequency waves and in larger pores or channels. In a pore scale, high-frequency waves may cause pore fluid to exhibit stiffer elastic behavior, which is commonly known as 'squirt flow' (Batzle et al., 2006; Müller and Gurevich, 2004; Tisato et al., 2021). It is observed that the changes in velocity at different stress conditions caused by dispersion cannot be justified uniformly with the squirt-flow model (Ba et al., 2024; Tisato et al., 2021). During an injection scenario, when the pore pressure is significantly low and starts increasing gradually, the decrease in Vp can be explained by a modified acousto-elasticity model incorporating Mori-Tanaka scheme and crack density model (David and Zimmerman, 2012; Mori and Tanaka, 1973). This closely follows a stress-dependent linear change in velocity. At seismic frequency, the physics remains the same, however the effect of squirt flow is less pronounced. Absolute magnitude of Vs shows minimal deviation with dispersion, however, Vp is much higher for saturated porous rocks at higher frequencies. When pore pressure approaches the confining pressure, the rate of velocity drop accelerates can be better explained by the squirt-flow model, since more channels and pore spaces are filled with pore fluids and there is higher chance of the pore fluid exhibiting a 'stiff' behavior (Ba et al., 2024). As expected, their experimental results indicate stronger influence of squirt-flow at ultrasonic frequency and vice versa. Additionally, the increase in pore pressure results in a proportionally faster decrease in velocity in both seismic and ultrasonic Vp, which is also evident in our ultrasonic experimental findings (Fig. 8a). Changes in Vs is also pore pressure-dependent, but is less affected by squirt-flow mechanism (Fig. 8b).

On the other hand, multiple studies reported contrasting response in wave velocities due to imbibition and drainage of non-wetting phases (Knight and Nolen-Hoeksema, 1990; Li et al., 2001; Mavko and Nolen-Hoeksema, 2012b). Fluid imbibition and drainage processes, especially of different wetting behavior is often complicated and hard to fit in a generalized physics. Various research indicates that the velocity change during imbibition of non-wetting phase is often sudden. There is negligible change in velocity in low saturation and a sudden change at a smaller saturation interval. This behavior is often attributed to the residual fluid distribution in sandstone (varies between 10–40 %) which depends on particle size, pore size and structure, grain contact etc. (Wilson and Conrad, 1984). Bacri and Salin, (1986) also pointed out that the change in velocity is more gradual when miscible phases (vapor against water) are displaced. In our experiments, liquid CO_2 is a non-wetting phase in brine saturated sandstone in stage D, which causes similar change.

Si et al. (2016) demonstrated that increase in saturation in sandstone cause pulsed and exponential increase in Vp and comparatively nominal increase in Vs. Gassman-Biot and Gassman-Hill theories also indicate a decrease in Vp at low saturation, followed by rapid increase which could also be observed in some of our coreplugs (Fig. 9). More pronounced changes in velocity and amplitudes could be seen in high porosity coreplugs, however, other petrophysical properties (grain size, permeability, mineralogy) of these specimens were different, which led to an inconclusive correlation between porosity and magnitude of velocity change. In Stage C of our experiments, we increase brine injection pressure, which causes first a quick increase in Vp, Vs and then remains constant (Fig. 10), possibly due to reduction in effective stresses.

4.6. Key indicators for reservoir-scale CO_2 injection monitoring

As mentioned before, the objective of this study was to find out the velocity and amplitude change pattern during different stages of CO_2 injection in a depleted saline aquifer. Displacement of brine by CO_2 which is expected during CO_2 injection, causes decrease in velocity and amplitudes, whereas irreversible deformation in a reservoir can also give similar indications. This study is also aimed to refine the traffic-light protocol proposed in Chandra et al. (2025) and give more robust information on the difference between stress induced velocity changes and fluid injection induced velocity changes. In order to avoid false indicator in monitoring, the traffic light system needs to be more robust so that we can differentiate effect of fluid and effect of stress. In the experiments discussed above, increase in Vs in Stage B is caused by elastic deformation of the coreplugs, where pore pressure remains constant. In Stage C, stress and corresponding velocity change is caused by pore pressure. Finally in Stage D, there is no stress change, but displacement of brine by liquid CO_2. We observed very different velocity and amplitude response

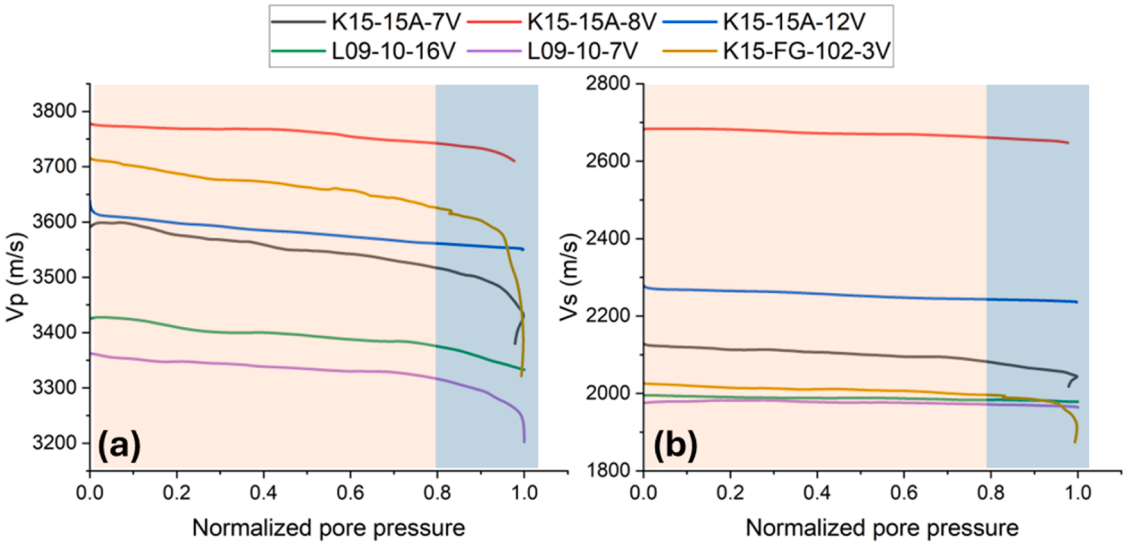

Fig. 8. Stage E of the triaxial experiments showing (a) Vp and (b) Vs drop with increase in pore pressure leading to failure. Since the pore pressure required for failure varies for different coreplugs, we normalize the values to make them comparable. The orange shaded zone represent velocity drop following acoustoelastic principle, whereas the blue shaded zone represent squirt-flow dominated velocity drop. K15-12-5 V is excluded since there were very few representative datapoints in Stage E.

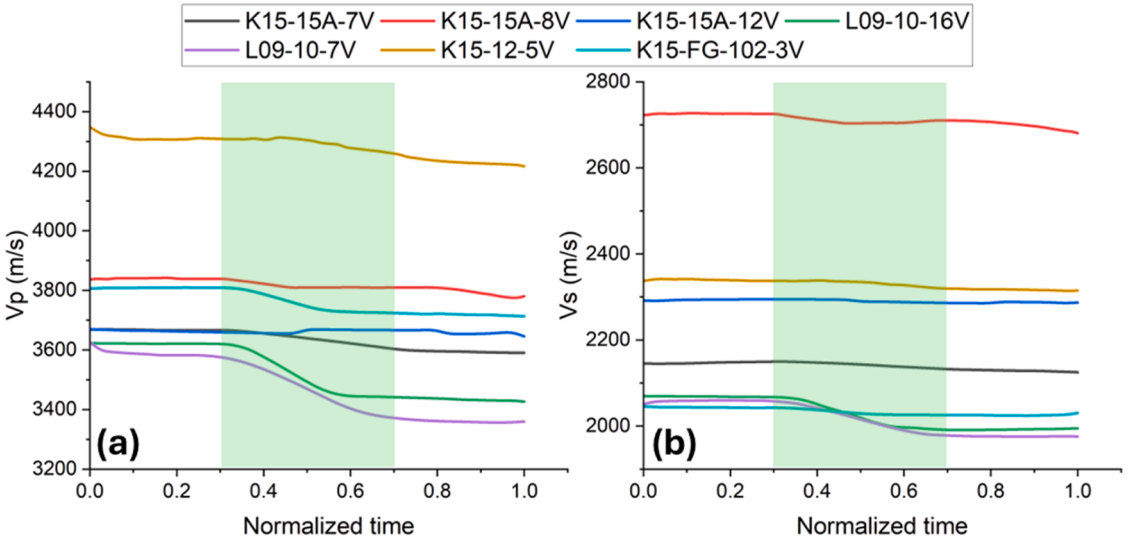

Fig. 9. The drop in (a) Vp and (b) Vs during liquid CO_2 flushing in brine saturated sandstone (Stage D). The time axis is normalized to make the data comparable across different samples. The green shaded zone indicates the period where a rapid drop in velocity was observed.

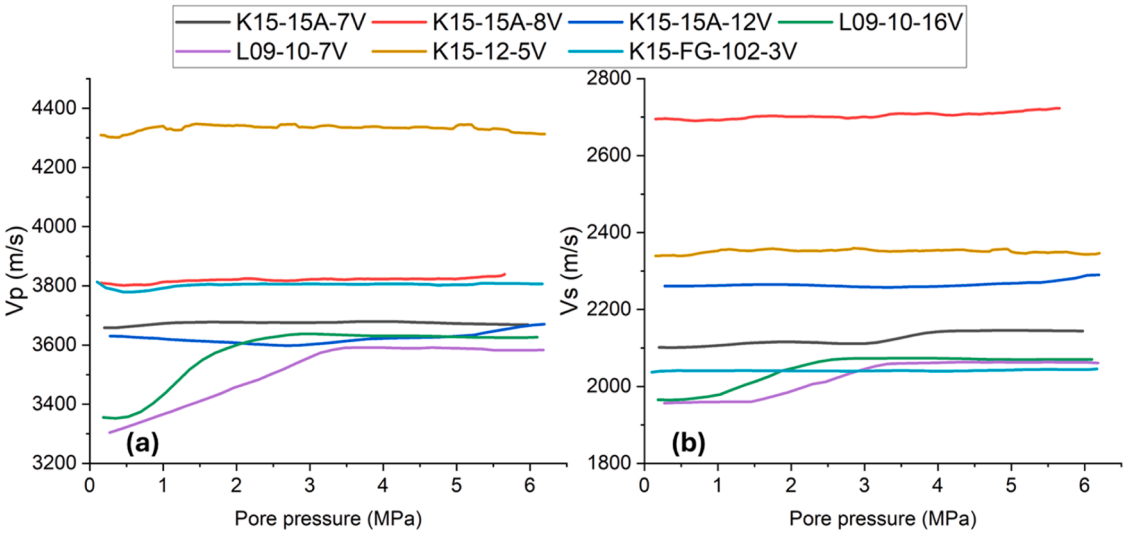

Fig. 10. Increase in (a) Vp and (b) Vs during Stage C of the triaxial tests due to increase in pore pressure with brine.

Table 2
Metrics indicating change in Vs, Samp and their ratio across different stages of the experiments. =Pp and +Pp indicates pore pressure unchanged and pore pressure increasing respectively.

Sample ID		K15-15A-7V	K15-15A-8V	K15-15A-12V	L09–10-16V	L09–10-7V	K15-12-5V	K15-FG-102-3V
Porosity (%)		11	9	14	13	23	11	17
Stage B (=Pp)	Vs*	6.36	8.39	3.64	1.85	1.97	1.71	1.99
	Samp*	4.7	5.59	4.85	4.76	6.12	12.2	18.3
	Samp*/Vs*	0.74	0.67	1.33	2.57	3.11	7.13	9.2
Stage C (+Pp)	Vs*	8.04	6.52	5.87	14.64	14.33	5.84	1.53
	Samp*	30.26	34	36	100	118	67	45
	Samp*/Vs*	3.76	5.21	6.13	6.83	8.23	11.47	29.41
Stage D (=Pp)	Vs*	-1.34 %	-1.87 %	-2.24 %	-4.06 %	-4.41 %	-1.39 %	-1.2 %
	Samp*	-45.72 %	-39.7 %	-20.14 %	-215.69 %	-327.01 %	-81.54 %	-31.08 %
	Samp*/Vs*	34.04	21.28	9	53.13	74.12	58.48	25.81
Stage E (+Pp)	Vs*	3.84	5.42	6.81	1.93	2.56	–	2.71
	Samp*	-1.66	-1.42	-2.54	-1.00	-1.06	–	-2.50
	Samp*/Vs*	-0.43	-0.26	-0.37	-0.52	-0.41	–	-0.92

in all three cases with shear waves (Table 2). Here we calculate the change in Vs and Samp per unit pressure change across all stages. The new terms Vs* and Samp* are expressed as follows (eq 1 and 2):

$$V_s^* = \frac{Vs_{max} - Vs_{min}}{\sigma^{eff}{}_{Vsmax} - \sigma^{eff}{}_{Vsmin}} \quad (1)$$

$$Samp^* = \frac{Samp_{max} - Samp_{min}}{\sigma^{eff}{}_{Vsmax} - \sigma^{eff}{}_{Vsmin}} \times 10 \quad (2)$$

For convenience in comparing, a multiplication factor of 10 is included in Samp*. Here Samp values are considered in mV. $\sigma^{eff}{}_{Vsmax/min}$ indicates the effective axial stress at Vs_{max} and Vs_{min}. It is worth mentioning that in Stage D, there was no stress change, so the changes in Vs and Samp are calculated as percentage.

The rate of increase in Vs due to pore pressure increase, even while the coreplugs are in plastic deformation regime, overpowers the rate of increase in Vs during elastic compression. The difference is even more significant for Samp, which is significantly affected by pore pressure increase. Intuitively the rate of change of Samp Vs is faster when there is influence of pore fluid. Whereas in Stage D, where there was no stress change, Vs showed minor decrease due to CO_2 imbibition, however, Samp decreases significantly compared to previous stages. In the final stage leading to failure, Vs decreases, but Samp shows minor increase until close to failure. We excluded the last few datapoint from this calculation where axial strain increases exponentially, since in context of CO_2 injection, failure (or situations close to failure) is rare. Here due to the opposite trend in Vs* and Samp*, their ratio is negative, which could act as a major indicator for CO_2 pressure increase leading to plastic deformation during field scale operation. It has been demonstrated that modern cross-well active seismic monitoring can detect extremely small variation (order of nanoseconds) in seismic travel times, making minor stress or fluid induced velocity or attenuation change easy to detect (Crampin, 2001; Silver et al., 2007). In Frio II seismic monitoring test, despite having noisy data due to fluid sampling, massive stacking of continuous waveforms enabled clear detection of 2–8 % changes in travel time every 15 mins due to CO_2 plume movement (Daley et al., 2007). The benefit of stacking and good background VSP data to identify plume movement was also iterated in the Citronelle Alabama CO_2 storage demonstration (Trautz et al., 2020). Marchesini et al. (2017) conducted continuous active source monitoring in Cranfield DAS site to measure injection pressure at different depth intervals with high accuracy using 10 tubing-deployed hydrophones and 2 piezoelectric seismic sources. They concluded that there is strong correlation between travel time and pore pressure with a uncertainty of 26 m in pore pressure distribution across depth. Crosswell seismic monitoring in the Aquistore CO_2 store project reported an even higher accuracy of CO_2 plume movement (5–10 m) and emphasized on velocity and amplitude changes as well as scattering due to plume migration (White et al., 2014). Many related studies have demonstrated excellent resolution in velocity and spectral change stress change and plume migration during CO_2 injection using crosswell active seismic (using geophone or fiber optics) and compared its efficiency with electromagnetic and 3D seismic surveys (Ajo-Franklin et al., 2013; Angerer et al., 2000; Daley et al., 2008a, 2017; Um et al., 2020). Therefore indicators like Vs* and Samp* proposed in this study can be determined even based on small changes in pore pressure and fluid displacement (e.g in the early stage of CO_2 injection, it should be easy to distinguish the magnitude and rate at which the pressure front and fluid front is moving).

To assess the correlation between stress change and acoustic properties more critically across different samples, we determined the Spearman rank correlation across different stages. Spearman rank correlation is a non-parametric measure of the strength and direction of the monotonic relationship between two variables, in this case percentage change in each indicator within each stage (Spearman, 1904). The correlation coefficient varies from -1 to +1 for perfectly negative and perfectly positive correlations respectively. Fig. 11a shows the parameter matrix of Stage B for K15-15A-7 V, and similar matrices were made for each stage and each experiment (Fig. S1). However, the first parameter varies across the stages. For stage B the first parameter is percentage change in axial stress, for stage C and E percentage change in pore pressure. However, in stage D, there was no apparent changes in effective stress, so no stress-term was considered for the ranking. In this stage, liquid CO_2 was injected at a constant flow rate, so percentage change in time was considered as a replacement for stress. In stage B, only the elastic loading part was considered, as the linear relationship between stress and acoustic indicators reverse after the onset of plasticity. Similarly, in stage E, data beyond the point of exponential strain increase is not considered for ranking. Fig. 11b indicates the average Spearman correlation rank determined within each stage (e.g the absolute average of all ranks in Fig. 11a). Any rank above 0.6 (dotted line) is assumed to be a good correlation and vice versa. We can see a consistent high rank in stage B, where acoustic indicators are only a function of axial loading. Except K15-15A-8 V and K15-12-5 V, all samples show a high rank in stage C and D and interestingly these two

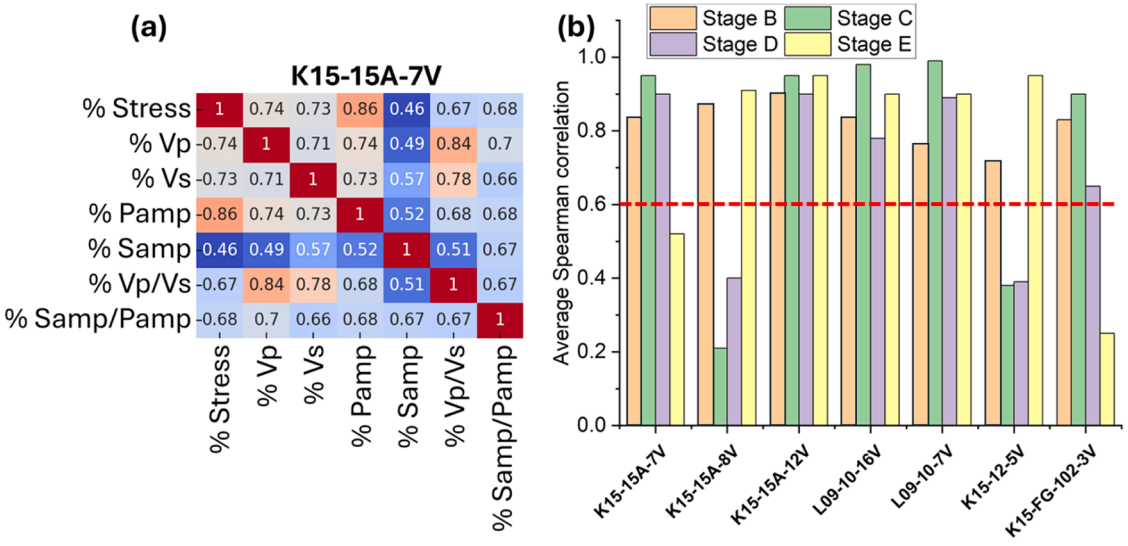

Fig. 11. (a) Spearman rank correlation of stress change and acoustic parameters in stage B for K15-15A-7 V. Stronger correlation is indicated by warmer colors and vice versa. (b) Average Spearman rank correlation for all stages in all experiments with the dotted line acting as a threshold for categorizing good and bad correlation.

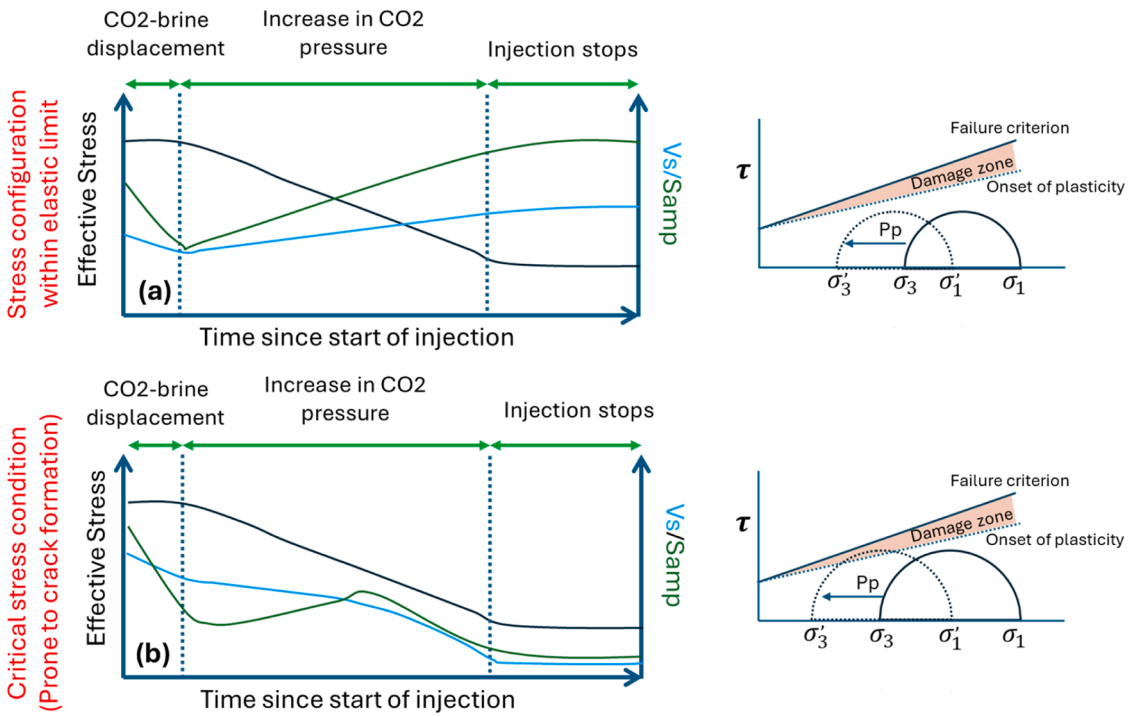

Fig. 12. A simple schematic of expected shear wave velocity and amplitude change during different timeframe of CO_2 injection in a (a) reservoir within elastic limit and (b) reservoir in critical stress condition. The Mohr circles on the right represent the stress configuration in each case.

are samples with the least initial permeability and comparatively low porosity (Table 1).

Based on our observations, the reservoir stress configuration, Vs and Samp can be linked and can act as strong monitoring tool for assessing safe CO_2 injection (Fig. 12). Having a clear idea about the reservoir stress configuration is crucial before making such assessments. In section 4.5 we also discussed how observations from seismic frequency and ultrasonic frequency are similar in many cases, albeit of different magnitude. Therefore, we present the monitoring protocol focusing more on the trend rather than the absolute values. Assuming the monitoring is taking place close to the injection well, and considering the reservoir stress conditions are well within the elastic limit, brine displacement by CO_2 in the starting phase of injection will cause minimal increase in pore pressure, but significant decrease in Samp and a gentler decrease in Vs (Fig. 12a). In a depleted saline aquifer, where CO_2 is stored in supercritical form, the drop in Samp and Vs will be greater during displacement of brine with CO_2 as density of liquid CO_2 > supercritical CO_2. A similar observation has been reported by Zhao et al. (2025) where they investigated the effect of fluid displacement and pore pressure on ultrasonic wave velocities and amplitudes using supercritical CO_2. After some time, depending on injection rate and permeability, pore pressure will start to increase, causing increase in CO_2 density, and a decrease in effective stresses- resulting in an increase in velocity and faster increase in amplitude. When we compare this to a critically stressed reservoir (i.e prone to irreversible deformation), the stress-velocity-amplitude correlations are a little more complicated (Fig. 12b). In the CO_2-brine displacement phase, Vs-Samp behaves similar to Fig. 12a, since the stress change is not applicable in that phase. However, when pore pressure starts increasing, the Mohr-Coulomb circle shifts more towards the failure criterion, going into the damage zone (characterized by the onset of plastic deformation) leading to more microcrack formation in the reservoir. This causes a slow decrease in Vs, however, Samp increases slowly initially due to the increase in density of pore fluid. After a certain point, when the rate of crack formation increases significantly, both Vs and Samp decreases at a faster rate. Compressibility of the pore fluids also significantly contributes to the density and therefore the amplitudes. Although we did not measure the compressibility of the brine used for these experiments, we know that water has negligible change in isothermal compressibility (β_{water} = 0.005 MPa^{-1}) across the experimental pressure range (Fine and Millero, 1973). Therefore, the brine used for this study is assumed to have a constant density with pore pressure. Liquid CO_2 on the other hand, has a non-linear decrease in isothermal compressibility ($\beta_{lCO2} = \frac{0.01}{P^{0.6}}$) within experimental pore pressure range (Aakre et al., 2021) (Fig. S2) where P is pore pressure. In a reservoir, assuming a 90°C isothermal condition, supercritical CO_2 will show a similar trend in compressibility ($\beta_{ScCO2} = \frac{0.015}{P^{0.75}}$), albeit with lower density (Aakre et al., 2021; Romei and Persico, 2021). Therefore, the increase in density of CO_2 is rapid at lower pore pressure, counterbalancing the possible decrease in amplitudes due to microcrack formation. At higher pore pressure, the increase in density is slower, therefore the impact of crack volume increase is more pronounced. The impact of density will be lower when the injected phase is brine/water (for geothermal projects) and more pronounced for compressible fluids like H_2.

5. Conclusions

The objective of this study was to demonstrate the applicability of compressional and shear waves for stress and plume migration monitoring in CO_2 injection operations, where at different stages of the project lifetime, stress change or fluid displacement or a both their coupled occurrence could be seen. However, more lab-scale and field-scale research needs be conducted on reservoirs having varying mineralogy and petrophysical properties, in order to improve confidence in the extent to which the results are representative. A critical assessment of differences in scale (reservoir instead of coreplugs), heterogeneity and wave attributes (seismic instead of ultrasonic) can help establish a link between experimental outcome and real-time monitoring. Based on our lab-scale experiments using ultrasonic wave attributes, we could derive the following key points which could be applicable for field scale monitoring:

1. Ultrasonic velocity and amplitudes increase linearly during elastic compaction. The rate of increase of shear wave velocity is higher compared to compressional waves, however, the trends in amplitude are opposite.
2. Fluid injection (imbibition of wetting and non-wetting fluids) causes pulsed increase (during pore pressure increase) or decrease (during CO_2-brine displacement) in ultrasonic velocity and amplitudes. This is caused by a combination of difference in capillary number, fluid wettability, porosity, pore connectivity and heterogeneity of the specimen. In low-frequency measurements, phenomena like wave induced flow and heterogeneities in the reservoir needs to be accounted for to calculate saturation from velocity change.
3. An increase in pore pressure under critically stressed conditions promotes crack formation, leading to a gradual decline in both P-wave (Vp) and S-wave (Vs) velocities, along with an exponential reduction in P-wave amplitude. In contrast, S-wave amplitude either remains constant or increases until reaching the failure threshold, after which it decreases sharply. Pore pressure changes in critical stress condition continuously changes the patch size and permeability due to pore collapse and crack formation, which needs to be studied in detail to upscale ultrasonic measurements to seismic scale.
4. The relative rate of increase in wave velocity and amplitude serves as a key indicator for distinguishing different scenarios, including plastic deformation independent of pore pressure, pore pressure-induced effective stress changes, CO_2-brine displacement, and pore pressure-induced plastic deformation. Monitoring these indicators over time enables operators to evaluate the reservoir's stress state and safety factor through cross-well or downhole seismic measurements. Since seismic waves are sensitive to microcracks and their directional anisotropy, velocity change due to inelastic deformation would be identifiable, however the exact magnitude of change would vary from our ultrasonic measurement and still needs to be investigated.
5. Applicability of this study extends beyond the scope of fluid injection operation, including subsurface CO_2, H_2 storage or geothermal applications, provided good background (before CO_2 injection) active seismic measurements are performed, and should be accompanied with other forms of monitoring (borehole pressure, distributed strain, geochemical) to achieve improved confidence on shape and extent of injected fluid plume.

CRediT authorship contribution statement

Debanjan Chandra: Writing – original draft, Visualization, Validation, Methodology, Investigation, Formal analysis, Data curation, Conceptualization. **Auke Barnhoorn:** Writing – review & editing, Validation, Supervision, Resources, Project administration, Funding acquisition.

Declaration of competing interest

The authors hereby declare no conflict of interest and that the work described has not been published previously, nor it is under consideration for publication elsewhere. The article's publication is approved by all authors before submission.

Acknowledgement

This publication has been produced with support from SHARP Storage (project no 327342). The SHARP project has been subsidized through ACT (EC Project no. 691712), by Rijksdienst voor Ondernemend Nederland (RVO). Marc Friebel, Jens van den Berg and Karel Heller are duly acknowledged for their technical support in preparing the samples and setting up the experiments. We acknowledge Shell and TNO for providing the samples and Kees Hindriks for the insightful discussions that helped us complete this study.

Supplementary materials

Supplementary material associated with this article can be found, in the online version, at doi:10.1016/j.ijggc.2025.104498.

Data availability

Data will be made available on request.

References

Aakre, S.R., Anderson, M.H., Brooks, P.W., 2021. Volumetric efficiency and pressure pulsations of a triplex reciprocating supercritical CO2 pump. J. Supercrit. Fluids. 168, 105072. https://doi.org/10.1016/J.SUPFLU.2020.105072.

Agofack, N., Lozovyi, S., Bauer, A., 2018. Effect of CO2 on P- and S-wave velocities at seismic and ultrasonic frequencies. Int. J. Greenh. Gas Control 78, 388–399. https://doi.org/10.1016/J.IJGGC.2018.09.010.

Ajo-Franklin, J.B., Peterson, J., Doetsch, J., Daley, T.M., 2013. High-resolution characterization of a CO2 plume using crosswell seismic tomography: Cranfield, MS, USA. Int. J. Greenh. Gas Control 18, 497–509. https://doi.org/10.1016/J.IJGGC.2012.12.018.

Alemu, B.L., Aker, E., Soldal, M., Johnsen, Ø., Aagaard, P., 2013. Effect of sub-core scale heterogeneities on acoustic and electrical properties of a reservoir rock: a CO2 flooding experiment of brine saturated sandstone in a computed tomography scanner. Geophys. Prospect. 61, 235–250. https://doi.org/10.1111/J.1365-2478.2012.01061.X.

Angerer, E., Crampin, S., Li, X.Y., Davis, T.L., 2000. Time-lapse seismic changes in a CO2 injection process in a fractured reservoir. SEG Tech. Program Expand. Abstr. 19, 1532–1535. https://doi.org/10.1190/1.1815700;PAGEGROUP:STRING:PUBLICATION.

Arts, R., Eiken, O., Chadwick, A., Zweigel, P., van der Meer, L., Zinszner, B., 2004. Monitoring of CO2 injected at Sleipner using time-lapse seismic data. Energy 29, 1383–1392. https://doi.org/10.1016/J.ENERGY.2004.03.072.

Ba, J., Wei, Y., Carcione, J.M., Adam, L., Tang, G., 2024. Stress and frequency dependence of wave velocities in saturated rocks based on acoustoelasticity with squirt-flow dissipation. Geophys. J. Int. 236, 1753–1763. https://doi.org/10.1093/gji/ggae020.

Bachrach, R., Busanello, G.B., Sayed, A., Branston, M., 2023. Surface distributed acoustic sensing. Emerg. Technol. CCS Site Monit. 2023, 1–3. https://doi.org/10.3997/2214-4609.202374035/CITE/REFWORKS.

Bacri, J.-C, Salin, D., 1986. Sound velocity of a sandstone saturated with oil and brine at different concentrations. Geophys. Res. Lett. 13, 326–328. https://doi.org/10.1029/GL013I004P00326.

Barnhoorn, A., Verheij, J., Frehner, M., Zhubayev, A., Houben, M., 2018. Experimental identification of the transition from elasticity to inelasticity from ultrasonic attenuation analyses. Geophysics 83, MR221–MR229. https://doi.org/10.1190/GEO2017-0534.1/ASSET/IMAGES/LARGE/FIGURE7.JPEG.

Batzle, M.L., Han, D.H., Hofmann, R., 2006. Fluid mobility and frequency-dependent seismic velocity - direct measurements. Geophysics 71. https://doi.org/10.1190/1.2159053/ASSET/IMAGES/LARGE/N1_1_F15.JPEG.

Berryman, J.G., 2012. Origin of Gassmann's equations. https://doi.org/10.1190/1.1444667 64, 1627–1629.

Berryman, J.G., 2004. Modeling high-frequency acoustic velocities in patchy and partially saturated porous rock using differential effective Medium theory. Int. J. Multiscale Comput. Eng. 2, 17. https://doi.org/10.1615/INTJMULTCOMPENG.V2.I1.80.

Brantut, N., Aben, F.M., 2021. Fluid pressure heterogeneity during fluid flow in rocks: new laboratory measurement device and method. Geophys. J. Int. 225, 968–983. https://doi.org/10.1093/GJI/GGAB019.

Bui, M., Adjiman, C.S., Bardow, A., Anthony, E.J., Boston, A., Brown, S., Fennell, P.S., Fuss, S., Galindo, A., Hackett, L.A., Hallett, J.P., Herzog, H.J., Jackson, G., Kemper, J., Krevor, S., Maitland, G.C., Matuszewski, M., Metcalfe, I.S., Petit, C., Puxty, G., Reimer, J., Reiner, D.M., Rubin, E.S., Scott, S.A., Shah, N., Smit, B., Trusler, J.P.M., Webley, P., Wilcox, J., Mac Dowell, N., 2018. Carbon capture and storage (CCS): the way forward. Energy Env. Sci 11, 1062–1176. https://doi.org/10.1039/c7ee02342a.

Cerasi, P., Stroisz, A., Sønstebø, E., Stanchits, S., Oye, V., Bauer, R., 2018. Experimental investigation of injection pressure effects on fault reactivation for CO2 storage. Int. J. Greenh. Gas Control 78, 218–227. https://doi.org/10.1016/J.IJGGC.2018.08.011.

Chalaturnyk, R., Zambrano, G., Soderberg, H., Lang, P., Lawton, D., Wichert, G., 2006. Integrated instrumentation system in an observation well for monitoring CO2 storage at the Penn West Pilot, Alberta, Canada. GHGT-8. Trondheim.

Chandra, D., Alghannam, L., Barnhoorn, A., 2025. Applicability of ultrasonic measurements to monitor and forecast stress change in subsurface storage applications. https://doi.org/10.2139/SSRN.5142677.

Chandra, D., Perez Salgado, B., Barnhoorn, A., 2024. Wave velocities as a proxy to forecast deformation during cyclic loading-unloading in porous reservoir rocks. EGUGA 4657. https://doi.org/10.5194/EGUSPHERE-EGU24-4657.

Chapman, S., Borgomano, J.V.M., Quintal, B., Benson, S.M., Fortin, J., 2021. Seismic wave attenuation and dispersion due to partial fluid saturation: direct measurements and numerical simulations based on X-ray CT. J. Geophys. Res. Solid. Earth. 126. https://doi.org/10.1029/2021JB021643 e2021JB021643.

Chapman, S., Borgomano, J.V.M., Yin, H., Fortin, J., Quintal, B., 2019. Forced oscillation measurements of seismic wave attenuation and stiffness moduli dispersion in glycerine-saturated Berea sandstone. Geophys. Prospect. 67, 956–968. https://doi.org/10.1111/1365-2478.12710.

Chapman, S., Tisato, N., Quintal, B., Holliger, K., 2016. Seismic attenuation in partially saturated Berea sandstone submitted to a range of confining pressures. J. Geophys. Res. Solid. Earth. 121, 1664–1676. https://doi.org/10.1002/2015JB012575.

Crampin, S., 2001. Developing stress-monitoring sites using cross-hole seismology to stress-forecast the times and magnitudes of future earthquakes. Tectonophysics. 338, 233–245. https://doi.org/10.1016/S0040-1951(01)00079-8.

Daley, T.M., Marchesini, P., Wilt, M., Cook, P., Freifeld, B.M., Lawton, D., 2017. Containment and monitoring institute-baseline geophysics for CO2 monitoring with crosswell seismic and electromagnetics. EAGE/SEG Research Workshop 2017 on Geophysical Monitoring of CO2 Injections: CCS and CO2-EOR, pp. 24–28. https://doi.org/10.3997/2214-4609.201701934/CITE/REFWORKS.

Daley, Thomas M., Myer, L.R., Peterson, J.E., Majer, E.L., Hoversten, G.M., 2008a. Time-lapse crosswell seismic and VSP monitoring of injected CO2 in a brine aquifer. Environ. Geol. 54, 1657–1665. https://doi.org/10.1007/S00254-007-0943-Z/FIGURES/11.

Daley, T.M, Sherlock, D., Freifeld, B., Sharma, S., 2008b. Otway project: multi-purpose borehole seismic sensors; design, installation and preinjection monitoring data. In: 7th Annual Conference on Carbon Capture and Sequestration.

Daley, T.M., Solbau, R.D., Ajo-Franklin, J.B., Benson, S.M., 2007. Continuous active-source seismic monitoring of CO2 injection in a brine aquifer. Geophysics 72. https://doi.org/10.1190/1.2754716/ASSET/IMAGES/LARGE/043705GPY4.JPEG.

Damani, A., Sondergeld, C.H., Rai, C.S., 2018. Experimental investigation of in situ and injection fluid effect on hydraulic fracture mechanism using acoustic emission in Tennessee sandstone. J. Pet. Sci. Eng. 171, 315–324. https://doi.org/10.1016/J.PETROL.2018.07.027.

Dasgupta, S., Kiyashchenko, D., Kudarova, A., Pawar, S., Hopkins, J., Devarakota, P., Wang, K., K, Sen, M., 2024. Prediction of CO2 saturation and elastic properties using capillary pressure-based rock physics model. SSRN Electron. J. https://doi.org/10.2139/SSRN.5068074.

David, E.C., Zimmerman, R.W., 2012. Pore structure model for elastic wave velocities in fluid-saturated sandstones. J. Geophys. Res. Solid. Earth. 117. https://doi.org/10.1029/2012JB009195.

De Jager, J., Geluk, M.C., 2007. Petroleum geology. In: Wong, T., Batjes, D., de Jager, J. (Eds.), Geology of the Netherlands. Royal Netherlands Academy of Arts and Sciences (KNAW), Amsterdam, pp. 241–264.

Diallo, M.S., Prasad, M., Appel, E., 2003. Comparison between experimental results and theoretical predictions for P-wave velocity and attenuation at ultrasonic frequency. Wave Motion. 37, 1–16. https://doi.org/10.1016/S0165-2125(02)00018-5.

Dutta, T.T., Otsubo, M., Kuwano, R., O'Sullivan, C., 2020. Evolution of shear wave velocity during triaxial compression. Soils Found. 60, 1357–1370. https://doi.org/10.1016/J.SANDF.2020.07.008.

Eid, R., Ziolkowski, A., Naylor, M., Pickup, G., 2015. Seismic monitoring of CO2 plume growth, evolution and migration in a heterogeneous reservoir: role, impact and importance of patchy saturation. Int. J. Greenh. Gas Control 43, 70–81. https://doi.org/10.1016/J.IJGGC.2015.10.019.

Falcon-Suarez, I.H., Papageorgiou, G., Jin, Z., Muñoz-Ibáñez, A., Chapman, M., Best, A.I., 2020. CO2-Brine substitution effects on ultrasonic wave propagation through sandstone with oblique fractures. Geophys. Res. Lett. 47. https://doi.org/10.1029/2020GL088439 e2020GL088439.

Fawad, M., Mondol, N.H., 2021. Monitoring geological storage of CO2: a new approach. Sci. Rep. 1–9. https://doi.org/10.1038/s41598-021-85346-8, 2021 11:1 11.

Feng, Xiating., 2017. Seismic monitoring of geological CO2 storage 421–447. https://doi.org/10.1201/B20406-14.

Filomena, C.M., Stollhofen, H., Van Ojik, K., 2012. High-resolution ultrasonic measurements as proxies to resolve clastic reservoir heterogeneity in a salt-cemented gas reservoir. Am. Assoc. Pet. Geol. Bull. 96, 1197–1209. https://doi.org/10.1306/01021211100.

Fine, R.A., Millero, F.J., 1973. Compressibility of water as a function of temperature and pressure. J. Chem. Phys. 59, 5529–5536. https://doi.org/10.1063/1.1679903.

Fortin, J., Schubnel, A., Guéguen, Y., 2005. Elastic wave velocities and permeability evolution during compaction of Bleurswiller sandstone. Int. J. Rock Mech. Min. Sci. 42, 873–889. https://doi.org/10.1016/J.IJRMMS.2005.05.002.

Frempong, P., Donald, A., Butt, S.D., 2007. The effect of pore pressure depletion and injection cycles on ultrasonic velocity and quality factor in a quartz sandstone. Geophysics 72. https://doi.org/10.1190/1.2424887/ASSET/IMAGES/LARGE/012702GPY15.JPEG.

Furre, A.K., Eiken, O., Alnes, H., Vevatne, J.N., Kiær, A.F., 2017. 20 Years of monitoring CO2-injection at Sleipner. Energy Procedia 114, 3916–3926. https://doi.org/10.1016/J.EGYPRO.2017.03.1523.

Furst, S., Chéry, J., Peyret, M., Mohammadi, B., 2020. Tiltmeter data inversion to characterize a strain tensor source at depth: application to reservoir monitoring. J. Geod. 94, 1–15. https://doi.org/10.1007/S00190-020-01377-5/FIGURES/8.

Gasperikova, E., Appriou, D., Bonneville, A., Feng, Z., Huang, L., Gao, K., Yang, X., Daley, T., 2022. Sensitivity of geophysical techniques for monitoring secondary CO2 storage plumes. Int. J. Greenh. Gas Control 114, 103585. https://doi.org/10.1016/J.IJGGC.2022.103585.

Gassman, F., 1951. Uber die elastizitat poroser medien. Vierteljahrsschr. Naturforschenden Ges. Zur. 96, 1–23.

Geluk, M.C., Röhling, H.G., 1997. High-resolution sequence stratigraphy of the Lower Triassic 'Buntsandstein' in the Netherlands and northwestern Germany. Geol. Mijnb. 76 (3), 227–246. https://doi.org/10.1023/A:1003062521373, 199776.

Guéguen, Y., Schubnel, A., 2003. Elastic wave velocities and permeability of cracked rocks. Tectonophysics. 370, 163–176. https://doi.org/10.1016/S0040-1951(03)00184-7.

Gurevich, B., Makarynska, D., de Paula, O.B., Pervukhina, M., 2010. A simple model for squirt-flow dispersion and attenuation in fluid-saturated granular rocks. GEOPHYSICS 75, N109–N120. https://doi.org/10.1190/1.3509782.

Hamada, G., Joseph, V., 2020. Developed correlations between sound wave velocity and porosity, permeability and mechanical properties of sandstone core samples. Pet. Res. 5, 326–338. https://doi.org/10.1016/J.PTLRS.2020.07.001.

Hangx, S., van der Linden, A., Marcelis, F., Bauer, A., 2013. The effect of CO2 on the mechanical properties of the Captain Sandstone: geological storage of CO2 at the Goldeneye field (UK). Int. J. Greenh. Gas Control 19, 609–619. https://doi.org/10.1016/J.IJGGC.2012.12.016.

Hu, L., Doetsch, J., Brauchler, R., Bayer, P., 2017. Characterizing CO2 plumes in deep saline formations: comparison and joint evaluation of time-lapse pressure and seismic tomography. Geophysics 82, ID1–ID18. https://doi.org/10.1190/GEO2016-0365.1/ASSET/IMAGES/LARGE/FIGUREC1.JPEG.

Hu, S., Li, X., Bai, B., Shi, L., Liu, M., Wu, H., 2017. A modified true triaxial apparatus for measuring mechanical properties of sandstone coupled with CO2-H2O biphase fluid. Greenh. Gases: Sci. Technol. 7, 78–91. https://doi.org/10.1002/GHG.1637.

Huang, F., Bergmann, P., Juhlin, C., Ivandic, M., Lüth, S., Ivanova, A., Kempka, T., Henninges, J., Sopher, D., Zhang, F., 2018. The first post-injection seismic monitor survey at the Ketzin pilot CO2 storage site: results from time-lapse analysis. Geophys. Prospect. 66, 62–84. https://doi.org/10.1111/1365-2478.12497/CITE/REFWORKS.

Hughes, D.S., Kelly, J.L., 1952. Variation of elastic wave velocity with saturation in Sandstone. Geophysics 17, 739–752. https://doi.org/10.1190/1.1437803.

Ivandic, M., Bergmann, P., Kummerow, J., Huang, F., Juhlin, C., Lueth, S., 2018. Monitoring CO2 saturation using time-lapse amplitude versus offset analysis of 3D seismic data from the Ketzin CO2 storage pilot site, Germany. Geophys. Prospect. 66, 1568–1585. https://doi.org/10.1111/1365-2478.12666/CITE/REFWORKS.

Janssen, M.T.G., Barnhoorn, A., Draganov, D., Wolf, K.H.A.A., Durucan, S., 2021. Seismic velocity characterisation of geothermal reservoir rocks for CO2 storage performance assessment. Appl. Sci. (Switz.) 11, 3641. https://doi.org/10.3390/APP11083641/S1.

Janssen, M.T.G., Draganov, D., Barnhoorn, A., Wolf, K.H.A.A., 2023. Storing CO2 in geothermal reservoir rocks from the Kizildere field, Turkey: combined stress, temperature, and pore fluid dependence of seismic properties. Geothermics. 108, 102615. https://doi.org/10.1016/J.GEOTHERMICS.2022.102615.

Kim, K., Makhnenko, R.Y., 2022. Short- and long-term responses of reservoir rock induced by CO2 injection. Rock. Mech. Rock. Eng. 55, 6605–6625. https://doi.org/10.1007/S00603-022-03032-1/FIGURES/9.

King, M.S., Marsden, J.R., 2012. Velocity dispersion between ultrasonic and seismic frequencies in brine-saturated reservoir sandstones. https://doi.org/10.1190/1.1451700 67, 254–258.

Knight, R., Dvorkin, J., Nur, A., 2012. Acoustic signatures of partial saturation. https://doi.org/10.1190/1.1444305 63, 132–138.

Knight, R., Nolen-Hoeksema, R., 1990. A laboratory study of the dependence of elastic wave velocities on pore scale fluid distribution. Geophys. Res. Lett. 17, 1529–1532. https://doi.org/10.1029/GL017I010P01529.

Kolkman-Quinn, B., Lawton, D.C., Macquet, M., 2023. CO2 leak detection threshold using vertical seismic profiles. Int. J. Greenh. Gas Control 123, 103839. https://doi.org/10.1016/J.IJGGC.2023.103839.

Komijani, M., Gracie, R., Sarvaramini, E., 2019. Simulation of induced acoustic emission in fractured porous media. Eng. Fract. Mech. 210, 113–131. https://doi.org/10.1016/J.ENGFRACMECH.2018.07.028.

Lawton, D., Couëslan, M., Bland, H., Chalaturnyk, R., Jones, M., 2006. Seismic survey design for monitoring CO2 storage: integrated multicomponent surface and borehole seismic surveys, Penn West Pilot, Alberta, Canada. In: Proc. of the 8th Int. Conf. on Greenhouse Gas Control Technologies, pp. 19–22.

Lebedev, M., Toms-Stewart, J., Clennell, B., Pervukhina, M., Shulakova, V., Paterson, L., Muller, T.M., Gurevich, B., Wenzlau, F., 2009. Direct laboratory observation of patchy saturation and its effects on ultrasonic velocities. Lead. Edge (Tulsa OK) 28, 24–27. https://doi.org/10.1190/1.3064142/ASSET/IMAGES/LARGE/24_1_F6.JPEG.

Li, X., Zhong, L., Pyrak-Nolte, L.J., 2001. Physics of partially saturated porous media: residual saturation and seismic-wave propagation. Annu Rev. Earth. Planet. Sci. 29, 419–460. https://doi.org/10.1146/ANNUREV.EARTH.29.1.419/CITE/REFWORKS.

Li, Z., Zuo, J., Sun, Y., Shi, Y., Ma, Z., 2022. Investigation on sandstone wave velocity variation and the stress response of pore structure. Bull. Eng. Geol. Environ. 81, 1–17. https://doi.org/10.1007/S10064-022-02723-X/FIGURES/14.

Lopes, S., Lebedev, M., 2012. Research note: laboratory study of the influence of changing the injection rate on the geometry of the fluid front and on P-wave ultrasonic velocities in sandstone. Geophys. Prospect. 60, 572–580. https://doi.org/10.1111/J.1365-2478.2011.01009.X/CITE/REFWORKS.

Lopes, S., Lebedev, M., Müller, T.M., Clennell, M.B., Gurevich, B., 2014. Forced imbibition into a limestone: measuring P-wave velocity and water saturation dependence on injection rate. Geophys. Prospect. 62, 1126–1142. https://doi.org/10.1111/1365-2478.12111/CITE/REFWORKS.

Marchesini, P., Ajo-Franklin, J.B., Daley, T.M., 2017. In situ measurement of velocity-stress sensitivity using crosswell continuous active-source seismic monitoring. Geophysics 82, D319–D326. https://doi.org/10.1190/GEO2017-0106.1/ASSET/IMAGES/LARGE/FIGURE6.JPEG.

Mathieson, A., Midgely, J., Wright, I., Saoula, N., Ringrose, P., 2011. In Salah CO2 Storage JIP: CO2 sequestration monitoring and verification technologies applied at Krechba, Algeria. Energy Procedia 4, 3596–3603. https://doi.org/10.1016/J.EGYPRO.2011.02.289.

Mavko, G., Nolen-Hoeksema, R., 2012a. Estimating seismic velocities at ultrasonic frequencies in partially saturated rocks. https://doi.org/10.1190/1.1443587 59, 252–258.
Mavko, G., Nolen-Hoeksema, R., 2012b Estimating seismic velocities at ultrasonic frequencies in partially saturated rocks. https://doi.org/10.1190/1.1443587 59, 252–258.
Mayr, S.I., Stanchits, S., Langenbruch, C., Dresen, G., Shapiro, S.A., 2011. Acoustic emission induced by pore-pressure changes in sandstone samples. Geophysics 76. https://doi.org/10.1190/1.3569579/ASSET/IMAGES/LARGE/6.JPEG.
Meglis, I.L., Chow, T., Martin, C.D., Young, R.P., 2005. Assessing in situ microcrack damage using ultrasonic velocity tomography. Int. J. Rock Mech. Min. Sci. 42, 25–34. https://doi.org/10.1016/J.IJRMMS.2004.06.002.
Michael, K., Avijegon, A., Ricard, L., Myers, M., Tertyshnikov, K., Pevzner, R., Strand, J., Hortle, A., Stalker, L., Pervukhina, M., Harris, B., Feitz, A., Pejcic, B., Larcher, A., Rachakonda, P., Freifeld, B., Woitt, M., Langhi, L., Dance, T., Myers, J., Roberts, J., Saygin, E., White, C., Seyyedi, M., 2020. A controlled CO2 release experiment in a fault zone at the In-situ Laboratory in Western Australia. Int. J. Greenh. Gas Control 99, 103100. https://doi.org/10.1016/J.IJGGC.2020.103100.
Mori, T., Tanaka, K., 1973. Average stress in matrix and average elastic energy of materials with misfitting inclusions. Acta Metall. 21, 571–574. https://doi.org/10.1016/0001-6160(73)90064-3.
Müller, T.M., Gurevich, B., 2004. One-dimensional random patchy saturation model for velocity and attenuation in porous rocks. https://doi.org/10.1190/1.1801934 69, 1166–1172.
Murdoch, L.C., Germanovich, L.N., DeWolf, S.J., Moysey, S.M.J., Hanna, A.C., Kim, S., Duncan, R.G., 2020. Feasibility of using in situ deformation to monitor CO2 storage. Int. J. Greenh. Gas Control 93, 102853. https://doi.org/10.1016/J.IJGGC.2019.102853.
Nur, A., Simmons, G., 1969. The effect of saturation on velocity in low porosity rocks. Earth. Planet. Sci. Lett. 7, 183–193. https://doi.org/10.1016/0012-821X(69)90035-1.
Ógúnsàmi, A.R., Jackson, I., Pimienta, L., Fortin, J., 2025. Squirt flow in a tight sandstone: an interlaboratory study. Geophys. J. Int. 240, 1387–1403. https://doi.org/10.1093/GJI/GGAE451.
Picotti, S., Carcione, J.M., Gei, D., Rossi, G., Santos, J.E., 2012. Seismic modeling to monitor CO2 geological storage: the Atzbach-Schwanenstadt gas field. J. Geophys. Res. Solid. Earth. 117, 6103. https://doi.org/10.1029/2011JB008540;CTYPE:STRING:JOURNAL.
Pimienta, L., Fortin, J., Guéguen, Y., 2015. Bulk modulus dispersion and attenuation in sandstones. Geophysics 80, D111–D127. https://doi.org/10.1190/GEO2014-0335.1.
Prasad, M., Glubokovskikh, S., Daley, T., Oduwole, S., Harbert, W., 2021. CO2 messes with rock physics. https://doi.org/10.1190/tle40060424.1 40, 424–432.
Qi, Q., Muller, T.M., Gurevich, B., Lopes, S., Lebedev, M., Caspari, E., 2014a. Quantifying the effect of capillarity on attenuation and dispersion in patchy-saturated rocks. Geophysics 79, WB35–WB50. https://doi.org/10.1190/GEO2013-0425.1.
Qi, Q., Müller, T.M., Rubino, J.G., 2014b. Seismic attenuation: effects of interfacial impedance on wave-induced pressure diffusion. Geophys. J. Int. 199, 1677–1681. https://doi.org/10.1093/gji/ggu327.
Rafieepour, S., Miska, S.Z., Ozbayoglu, E.M., Takach, N.E., Yu, M., Zhang, J., 2021. Experimental investigation of depletion- and injection-induced changes in poromechanical, transport, and strength properties of high-porosity sandstone. SPE J. 26, 2793–2813. https://doi.org/10.2118/205364-PA.
Ranjith, P.G., Perera, M.S.A., 2011. A new triaxial apparatus to study the mechanical and fluid flow aspects of carbon dioxide sequestration in geological formations. Fuel 90, 2751–2759. https://doi.org/10.1016/J.FUEL.2011.04.004.
Romei, A., Persico, G., 2021. Computational fluid-dynamic modelling of two-phase compressible flows of carbon dioxide in supercritical conditions. Appl. Therm. Eng. 190, 116816. https://doi.org/10.1016/J.APPLTHERMALENG.2021.116816.
Sang, G., Liu, S., Elsworth, D., 2020. Quantifying fatigue-damage and failure-precursors using ultrasonic coda wave interferometry. Int. J. Rock Mech. Min. Sci. 131, 104366. https://doi.org/10.1016/J.IJRMMS.2020.104366.
Sayers, C.M., Kachanov, M., 1995. Microcrack-induced elastic wave anisotropy of brittle rocks. J. Geophys. Res. Solid. Earth. 100, 4149–4156. https://doi.org/10.1029/94JB03134.
Scott, T.E., Ma, Q., Roegiers, J.C., 1993. Acoustic velocity changes during shear enhanced compaction of sandstone. Int. J. Rock Mech. Min. Sci. Geomech. Abstr. 30, 763–769. https://doi.org/10.1016/0148-9062(93)90020-E.
Sen, A., Dvorkin, J., 2013. Frequency effect in fluid substitution: capillary pressure equilibrium theory. In: SEG Annual Meeting. OnePetro, Houston. https://doi.org/10.1190/segam2013-0392.1.
Sevostianov, I., 2020. Gassmann equation and replacement relations in micromechanics: A review. Int. J. Eng. Sci. 154, 103344. https://doi.org/10.1016/J.IJENGSCI.2020.103344.
Si, W., Di, B., Wei, J., Li, Q., 2016. Experimental study of water saturation effect on acoustic velocity of sandstones. J. Nat. Gas. Sci. Eng. 33, 37–43. https://doi.org/10.1016/J.JNGSE.2016.05.002.
Silver, P.G., Daley, T.M., Niu, F., Majer, E.L., 2007. Active source monitoring of cross-well seismic travel time for stress-induced changes. Bull. Seismol. Soc. Am. 97, 281–293. https://doi.org/10.1785/0120060120.
Spearman, C., 1904. The proof and measurement of association between two things. Am. J. Psychol. 15, 72. https://doi.org/10.2307/1412159.
Stanchits, S.A., Lockner, D.A., Ponomarev, A.V., 2003. Anisotropic changes in P-wave velocity and attenuation during deformation and fluid infiltration of granite. Bull. Seismol. Soc. Am. 93, 1803–1822. https://doi.org/10.1785/0120020101.
Sun, W., 2021. On the theory of biot-patchy-squirt mechanism for wave propagation in partially saturated double-porosity medium. Phys. Fluids 33. https://doi.org/10.1063/5.0057354/1077243.
Sun, Y., Carcione, J.M., Gurevich, B., 2020. Squirt-flow seismic dispersion models: a comparison. Geophys. J. Int. 222, 2068–2082. https://doi.org/10.1093/GJI/GGAA274.
Tarokh, A., Makhnenko, R.Y., Kim, K., Zhu, X., Popovics, J.S., Segvic, B., Sweet, D.E., 2020. Influence of CO2 injection on the poromechanical response of Berea sandstone. Int. J. Greenh. Gas Control 95, 102959. https://doi.org/10.1016/J.IJGGC.2020.102959.
Tisato, N., Madonna, C., Saenger, E.H., 2021. Attenuation of seismic waves in partially saturated berea sandstone as a function of frequency and confining pressure. Front. Earth Sci. (Lausanne) 9, 641177. https://doi.org/10.3389/FEART.2021.641177/BIBTEX.
Trautz, R., Daley, T., Miller, D., Robertson, M., Koperna, G., Riestenberg, D., 2020. Geophysical monitoring using active seismic techniques at the Citronelle Alabama CO2 storage demonstration site. Int. J. Greenh. Gas Control 99, 103084. https://doi.org/10.1016/J.IJGGC.2020.103084.
Um, E., Marchesini, P., Wilt, M., Nichols, E., Alumbaugh, D., Vasco, D., Daley, T., 2020. Joint use of crosswell EM and seismics for monitoring CO2 storage at the Containment and Monitoring Institute Field Site (CaMI): baseline surveys and preliminary results. SEG Technical Program expanded abstracts 2020-October, 575–579. https://doi.org/10.1190/SEGAM2020-3427004.1.
Van Hulten, F.F.N., 2006. Reservoir quality distribution as tool for better exploration prospect evaluation and estimation of the resource base in the Netherlands. Tight Gas Fields Neth. Workshop EBN-TNO.
Van Stappen, J.F., Meftah, R., Boone, M.A., Bultreys, T., De Kock, T., Blykers, B.K., Senger, K., Olaussen, S., Cnudde, V., 2018. In situ triaxial testing to determine fracture permeability and aperture distribution for CO2 sequestration in Svalbard, Norway. Environ. Sci. Technol. 52, 4546–4554. https://doi.org/10.1021/ACS.EST.8B00861/ASSET/IMAGES/LARGE/ES-2018-00861S_0005.JPEG.
Veltmeijer, A., Naderloo, M., Barnhoorn, A., 2024. Precursors to rock failure in the laboratory using ultrasonic monitoring methods. Geomech. Geophys. Geo-Energy Geo-Resour. 10, 1–15. https://doi.org/10.1007/S40948-024-00812-7/FIGURES/9.
Wang, Z., Dilmore, R.M., Harbert, W., 2020. Inferring CO2 saturation from synthetic surface seismic and downhole monitoring data using machine learning for leakage detection at CO2 sequestration sites. Int. J. Greenh. Gas Control 100, 103115. https://doi.org/10.1016/J.IJGGC.2020.103115.
White, D., Daley, T.M., Paulsson, B., Harbert, W., 2021. Borehole seismic methods for geologic CO2storage monitoring. Lead. Edge 40, 434–441. https://doi.org/10.1190/TLE40060434.1/ASSET/IMAGES/LARGE/TLE40060434.1_FIG8.JPEG.
White, D.J., Roach, L.A.N., Roberts, B., Daley, T.M., 2014. Initial results from seismic monitoring at the Aquistore CO2 Storage Site, Saskatchewan, Canada. Energy Procedia 63, 4418–4423. https://doi.org/10.1016/J.EGYPRO.2014.11.477.
Will, R., Smith, V., Leetaru, H.E., Freiburg, J.T., Lee, D.W., 2014. Microseismic monitoring, event occurrence, and the relationship to subsurface geology. Energy Procedia 63, 4424–4436. https://doi.org/10.1016/J.EGYPRO.2014.11.478.
Wilson, J.L., Conrad, S.H., 1984. Is physical displacement of residual hydrocarbons a realistic possibility in aquifer restoration. In: Proceedings of the NWWA/API Conference on Petroleum Hydrocarbons and Organic Chemicals in Ground Water—Prevention, Detection, and Restoration. Houston.
Xing, H.Z., Wu, G., Dehkhoda, S., Ranjith, P.G., Zhang, Q.B., 2019. Fracture and mechanical characteristics of CO2-saturated sandstone at extreme loading conditions. Int. J. Rock Mech. Min. Sci. 117, 132–141. https://doi.org/10.1016/J.IJRMMS.2019.03.025.
Yamabe, H., Tsuji, T., Liang, Y., Matsuoka, T., 2016. Influence of fluid displacement patterns on seismic velocity during supercritical CO2 injection: simulation study for evaluation of the relationship between seismic velocity and CO2 saturation. Int. J. Greenh. Gas Control 46, 197–204. https://doi.org/10.1016/J.IJGGC.2016.01.011.
Zhang, Q., Ye, W., Chen, Y., Li, X., Hu, S., 2021. Mechanical behavior of sandstone pressurized with supercritical CO2 and water under different confining pressure conditions. Int. J. Geomech. 21, 04021100. https://doi.org/10.1061/(ASCE)GM.1943-5622.0002061.
Zhang, T., Zhang, W., Yang, R., Cao, D., Chen, L., Li, D., Meng, L., 2022. CO2 Injection deformation monitoring based on UAV and InSAR technology: a case study of Shizhuang Town, Shanxi Province, China. Remote Sens. 14, 237. https://doi.org/10.3390/RS14010237, 2022VolPage14, 237.
Zhang, Y., Jackson, C., Zahasky, C., Nadhira, A., Krevor, S., 2022. European carbon storage resource requirements of climate change mitigation targets. Int. J. Greenh. Gas Control 114, 103568. https://doi.org/10.1016/J.IJGGC.2021.103568.
Zhang, Y., Park, H., Nishizawa, O., Kiyama, T., Xue, Z., 2017. Fluid distribution effects on P-wave velocity of CO2/brine saturated rocks: a comparison study and implications for CO2 storage monitoring using seismic method. Energy Procedia 114, 3786–3792. https://doi.org/10.1016/J.EGYPRO.2017.03.1509.
Zhao, L., Zhao, Y., Song, X., Wang, Y., Chen, Y., Zhu, Z., Yang, R., Geng, J., 2025. An experimental study of the elastic properties of the sandstone flooded with supercritical CO_2: the influences of saturation, pressure and temperature. Geophys. J. Int. 241, 702–714. https://doi.org/10.1093/GJI/GGAF069.
Zheng, H., Feng, X.T., Pan, P.Z., 2015. Experimental investigation of sandstone properties under CO2–NaCl solution-rock interactions. Int. J. Greenh. Gas Control 37, 451–470. https://doi.org/10.1016/J.IJGGC.2015.04.005.
Zhu, S., Kang, J., Wang, Y., Zhou, F., 2022. Effect of CO2 on coal P-wave velocity under triaxial stress. Int. J. Min. Sci. Technol. 32, 17–26. https://doi.org/10.1016/J.IJMST.2021.09.006.
Zhu, T., Ajo-Franklin, J., Daley, T.M., Marone, C., 2019. Dynamics of geologic CO 2 storage and plume motion revealed by seismic coda waves. Proc. Natl. Acad. Sci. u S.

a 116, 2464–2469. https://doi.org/10.1073/PNAS.1810903116/SUPPL_FILE/PNAS.1810903116.SAPP.PDF.
Zhubayev, A., Houben, M.E., Smeulders, D.M.J., Barnhoorn, A., 2016. Ultrasonic velocity and attenuation anisotropy of shales, Whitby, United Kingdom. Geophysics 81, D45–D56. https://doi.org/10.1190/GEO2015-0211.1/ASSET/IMAGES/LARGE/FIGURE10.JPEG.
Zotz-Wilson, R., Boerrigter, T., Auke, Barnhoorn, Barnhoorn, A., 2019. Coda-wave monitoring of continuously evolving material properties and the precursory detection of yielding. J. Acoust. Soc. Am. 145, 1060–1068. https://doi.org/10.1121/1.5091012.